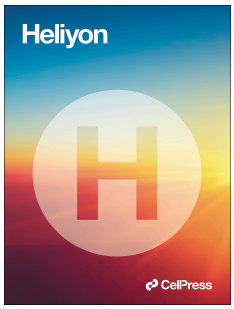

Fabrication of polymeric sorafenib coated chitosan and fucoidan nanoparticles: Investigation of anticancer activity and apoptosis in colorectal cancer cells

Yu Zhou, Jin Liu, Sai Ma, Xiaodong Yang, Zhenzhen Zou, Wen Lu, Tingjun Wang, Chunrong Sun, Chungen Xing

PII: S2405-8440(24)10347-7

DOI: https://doi.org/10.1016/j.heliyon.2024.e34316

Reference: HLY 34316

To appear in: *HELIYON*

Received Date: 18 May 2024

Revised Date: 26 June 2024

Accepted Date: 8 July 2024

Please cite this article as: Fabrication of polymeric sorafenib coated chitosan and fucoidan nanoparticles: Investigation of anticancer activity and apoptosis in colorectal cancer cells, *HELIYON*, https://doi.org/10.1016/j.heliyon.2024.e34316.

Fabrication of polymeric sorafenib coated chitosan and fucoidan nanoparticles: Investigation of anticancer activity and apoptosis in colorectal cancer cells

Yu Zhou[1,2,#], Jin Liu[3,#], Sai Ma[4], Xiaodong Yang[1], Zhenzhen Zou[5], Wen Lu[2], Tingjun Wang[2], Chunrong Sun[2*],Chungen Xing[1*]

[1]Department of General Surgery, The Second Affiliated Hospital of Soochow University, Suzhou 215000, Jiangsu Province, China.

[2]Department of General Surgery, The Affiliated Suzhou Hospital of Nanjing Medical University, Suzhou Municipal Hospital, Gusu School, Nanjing Medical University, Suzhou 215000, Jiangsu Province, China.

[3]Department of Infectious Diseases, The Affiliated Infectious Diseases Hospital, Suzhou Medical College of Soochow University, The Fifth Hospital of Suzhou, Suzhou 215000, Jiangsu Province, China.

[4]Department of Central Laboratory, The Affiliated Suzhou Hospital of Nanjing Medical University, Suzhou Municipal Hospital, Gusu School, Nanjing Medical University, Suzhou 215000, Jiangsu Province, China.

[5]Department of Laboratory, The Fourth Affiliated Hospital of Soochow University, Dushuhu Public Hospital Affiliated to Soochow University, Suzhou 215000, Jiangsu Province, China.

#contributed equally to this study

***Correspondence to:**

Chungen Xing, 1055 Sanxiang Road, Suzhou 215000, Jiangsu Province, China.

Chunrong Sun, 242 Guangji Road, Suzhou 215000, Jiangsu Province, China.

Abstract

The most prevalent form of colon cancer also ranks high among cancer-related deaths globally. Traditional chemotherapy drugs do not provide sufficient therapeutic efficacy, and advanced colon cancer demonstrates considerable resistance to chemotherapy. As an oral kinase inhibitor, sorafenib (SOR) suppresses the growth of tumour cells, the formation of new blood vessels, and the death of cancer cells. Unfortunately, sorafenib's limited bioavailability, rapid metabolism, and poor solubility have severely limited its clinical use. We developed nanoparticles targeting P-selectin and SOR, with fucoidan (FU) as a ligand. The SOR-CS-FU-NPs were developed by coating polylactide-co-glycolide nanoparticles with chitosan and FU through electrostatic interaction. The SOR-CS-FU-NPs exhibited an average particle diameter of 209.98 ± 1.25 nm and a polydisperse index (PDI) of 0.229 ± 0.022. The SOR-CS-FU nanoparticles exhibited a continuous release pattern for up to 120 h. The SOR-CS-FU nanoparticles exhibited cytotoxicity 8 times greater than free SOR in HCT116 colorectal cancer cells. The cellular absorption of Rhodamine-CS-FU-NPs was three times more than that of free Rhodamine and 19 times greater than that of Rhodamine-CS-NPs. Enhanced reactive oxygen species (ROS) generation and mitochondrial membrane potential damage were also shown in SOR-CS-FU-NPs. An investigation of cell death found that SOR-CS-FU-NPs had an apoptosis index that was 7.5 times greater than free SOR. After that, the SOR-CS-FU-NPs demonstrated a more significant inhibition of cell migration, leading to a wound closure of about 5%. No toxicity was shown in the non-cancer VERO cell line when exposed to the developed NPs. Taken together, these results provide strong evidence that biocompatible SOR-CS-FU-NPs fabricated effective carriers for the targeted delivery of dasatinib to colorectal cancer.

Keywords: Fucoidan; Chitosan; P-selectin; Sorafenib; Colorectal cancer; Apoptosis

Introduction

A highly graded hemangioma is a common way to diagnose colon cancer, the third most deadly form of cancer in the world. As a possible treatment for colon cancer, anti-angiogenic techniques have been proposed to fight this disease [1]. Chemotherapy, along with other cancer treatments, including radiation and surgery, is among the most prevalent ways that patients are treated [2]. Nevertheless, there are several drawbacks to many traditional anticancer drugs. These include low blood circulation, lack of cell-specificity, and poor water solubility [3–5]. Several advantages, including improved water solubility of chemo drugs, higher cellular uptake, prolonged blood circulation time, and enhanced tumour accumulation, have made nanoparticle-based drug carriers a hot topic in cancer chemotherapy [6,7]. Among the several colon cancer treatments available, the multikinase inhibitor sorafenib (SOR) can significantly increase patients' chances of survival by blocking the formation of new blood vessels [8–10]. Unfortunately, SOR still has a few issues due to its short half-life in vivo and limited water solubility [11]. The fact that colon cancer has the potential to develop resistance to SOR and avoid anti-angiogenic treatment means that it has a high recurrence rate. For this reason, novel approaches to resolving these issues are crucial [12]. Nanoparticles with precise targeting qualities can be designed and prepared to limit hazardous side effects on normal tissues while improving drug accumulation in malignant tissues [13]. Targeted nanoparticles can selectively administer drugs by focusing on particular antigens or receptors on the surface of cancer cells [13,14].

Much study has been conducted on biodegradable polymeric nanocarriers to increase the solubility of hydrophobic drugs, extend their half-life, and enhance the targeted enrichment efficiency of drugs to tumours through the improved penetration and retention (EPR) effect [15–17]. Nanoscale drug carriers, with characteristics like high selective accumulation in tumours via the enhanced permeability and retention (EPR) effect and active cellular uptake, have shown promise to address some of these challenges compared to conventional chemotherapeutic agents [18]. This is because they can improve treatment efficacy while avoiding toxicity in normal cells. Conjugating

compounds that bind to overexpressed antigens with nanocarriers delivering chemotherapeutics can enable active targeted approaches [19]. Nanodrug Genexol®-PM, for instance, has been available to the public; it uses an amphiphilic biodegradable block copolymer to encapsulate the anticancer drug paclitaxel. Patients with breast cancer, non-small cell lung cancer, and ovarian cancer have benefited from the nano drug's ability to increase paclitaxel's effectiveness while decreasing the drug's detrimental effects [20]. Several issues with nanodrugs are common to other polymeric micelles that self-assemble from block copolymers. First, although polymeric micelles self-assembled from amphiphilic polymers are relatively durable beyond the critical micelle concentration (CMC) in vitro, they may dissociate fast after injection into the body due to the considerable dilution. Secondly, because the stability of nanocarriers is also dependent on the interaction between hydrophobic regions and the drug, their early release into circulation can reduce delivery efficiency [21]. Premature circulatory release and decreased delivery efficiency are consequences of poor interactions between numerous chemotherapeutic drugs and polymers. Lastly, regular nanocarriers of PLGA are ineffective against cancer drugs that cause resistance [22,23]. Thus, it is highly beneficial to develop novel nanocarriers that can enhance the in vivo stability of the vector, efficiently load drugs, and circumvent cancer drug resistance [24]. Although the drug shows promise as an anticancer treatment in several trials, its poor delivery qualities constitute a significant drawback. It can significantly enhance the drug's prospective therapeutic applications by developing a nanoparticle or colloidal drug delivery technology that permits drug administration in water [25]. Many first-line chemotherapeutic drugs are investigated for potential drug delivery carriers, focusing on natural products and polymeric NPs [26]. A few nano-formulations are now being studied in clinical settings, and PLGA has already been approved for use in cancer treatment when combined with chemotherapeutic drugs. Drug delivery by PLGA nanoparticles is, thus, a viable alternative and an exciting new direction in cancer treatment [27].

Polysaccharides that serve biological purposes are gaining popularity due to their strong ability to stimulate the immune system [28]. Tissue engineering extensively uses

polysaccharide-based polymers, exhibiting potential as transporters for drugs and nucleic acids [29–33]. A brown seaweed extract called fucoidan is an anionic polysaccharide mainly composed of L-fucopyranose units and sulfated ester groups [34–36]. Investigations have shown that fucoidan can inhibit the growth of many different types of cancer in humans. Numerous biological and clinical studies have examined fucoidan's possible anti-inflammatory, antithrombotic, and anticoagulant effects [37–39]. In response to stimuli, cells such as activated platelets, endothelial cells, and metastatic tumours express P-selectin [40–42]. A P-selectin-targeted ligand called fucoidan selectively blocked platelet adherence [43–46]. Many human cancers express P-selectin, which fucoidan-based nanoparticles (hydrazide-PEG-hydrazide/fucoidan NPs) can also target [42].

The current study used SOR-loaded PLGA NPs (SOR-NPs) to increase drug loading, enhance solubility, and impart biocompatibility. The conjugation procedure that attaches FU adds complexity, extra steps, and the possibility that the final formulation will retain solvent residues (**Figure 1**). This led us to employ electrostatic contact to develop multi-layered NPs. To develop SOR-CS-FU-NPs, CS was first applied to negatively charged SOR-NPs, and then FU was used to coat the CS. Extensive physicochemical property optimization and in vitro release behaviour were performed on the formulation. To evaluate the SOR-CS-FU-NPs' in vitro efficacy, the HCT116 cell line was utilized since this type of cell is known to exhibit relatively high levels of P-selectin receptors. The targeting ability and anticancer efficacy of SOR-CS-FU-NPs were impressively demonstrated in the in-vitro investigations.

Experimental section

Materials and reagents

Sorafenib (SOR), chitosan (CS), and fucoidan (FU) were purchased from TCI and Sigma-Aldrich. Polylactide-co-glycolide (PLGA), Tocopherol polyethylene glycol succinate (TPGS), and MTT cytotoxicity assay kits for cell viability detection were bought from Thermo Fisher Scientific. Hoechst and lysotracker (green) were purchased from Beyotime Biotechnology (Shanghai, China). The staining kits were purchased from Qiyue

Biotechnology Co., Ltd. Solvents were either purchased or dried according to procedures described in the literature. Ultrapure water was obtained using a Milli-Q purification system.

Preparation of SOR-NPs

PLGA (1 ml) in acetone (5 mL) and a SOR solution (5 ml) in a 50:50 mixture of acetonitrile and methanol were mixed. While swirling vigorously, the resulting mixture was slowly added dropwise to a water solution that contained Tween 80. Additionally, swirling at 1000 revolutions per minute (RPM) for 2.5 h evaporated at the organic solvents at 65 ^{o}C. At a concentration of 0.5 %, we tested the effects of many surfactants on average NP size and PDI. These surfactants included PVA, Pluronic F-127, Tween 80, and TPGS. In addition, it was optimized at different concentrations of the chosen surfactant, including 0.1, 0.5, 0.75, and 1%. The physicochemical properties of NPs changed when the solvent-to-antisolvent ratio and the drug-to-polymer ratio (1:5, 1:10, 1:12, and 1:15). We measured whether PDI, % EE, and average NP size changed as drug concentration increased. Similarly, Rhodamine (Rh) loaded NPs were prepared using the above process wherein Rhodamine (Rh) was added in the organic phase instead of SOR.

Preparation of SOR-CS-NPs and SOR-CS-FU-NPs

An electrostatic coating was applied to the CS layer to achieve a positive charge on the surface of the NP [47]. Dissolving CS in 1% acetic acid and mixing at room temperature allowed us to make solutions of various concentrations. SOR-NPs (3 mL) were continuously mixed with CS solutions in varying concentrations (0.1, 0.2, 0.5, and 1.0 %). For 1 h, while stirring continuously, the NP above dispersion was incubated with CS solution.

Physicochemical characterization of NPs

A DLS analyzer determined the sizes of the nanoformulations (Zetasizer Nano ZS90 Malvern Instruments, Malvern) with a detection angle of 90° at 25°C using an incident He-Ne laser (λ = 633 nm). The high-performance liquid chromatography (HPLC) analysis was

conducted on an Agilent1200 machine (Agilent, USA). A JEM-2100 microscope obtained transmission electron microscopy (TEM) images at an acceleration voltage of 200 kV. A Bruker D8 Advance collected powder X-ray diffraction (XRD) data with a 6° / min scan rate. FT-IR analysis was recorded on a Fourier transform infrared spectrometer (Bruker, VERTEX 70). The surface and the size topography of the SOR-CS-FU-NPs were examined with AFM. A thin sample film was prepared on a cover slip by dropping 0.1 mL of the sample on the slide and drying for 30 min. The slide was scanned with AFM (APE Research-Model No: A100SGS), and high-resolution surface images were produced.

In-vitro drug release

The dialysis bag (MWCO 12 kDa) was loaded with optimal SOR-CS-FU-NPs, SOR-NPs, and free SOR. Phosphate buffer saline (PBS) at a pH of 7.4 and 0.5% Tween 80 was used to suspend the bags. The suspension medium and dialysis bags were mixed in an orbital shaker with beakers stirred at 100 rpm and 37 ± 0.5 °C. At intervals of up to 120 h, the aliquots were removed from the media and replaced with fresh media of the same volume to keep the volumes constant. Utilizing the established HPLC technique, the amount of SOR released was estimated [48]. Data are presented as mean ± standard deviation (SD) (n=3).

Cytotoxicity assay

HCT116 (human colon cancer cell line) and non-cancer VERO cell line were purchased from ATCC. The cells were routinely grown in RPMI medium added with 10% FBS, 100 U/ml penicillin, and 100 µg/ml streptomycin.

We evaluated the in vitro cytotoxicity of the SOR-CS-FU-NPs, SOR-NPs, and free SOR (5, 10, 20, 40, 60, and 80 µg/mL) via standard MTT cell viability assays. HCT116 cells and VERO cells were seeded into each well of a 96-well plate with a density of 1×10^3 cells per well in 0.1 mL DMEM and cultured overnight. The next day, the cells were washed three times with PBS and incubated with fresh medium containing SOR-CS-FU-NPs, SOR-NPs, and free SOR at different concentrations at 37 ^{o}C for 24 h. The viability of cells treated with HCT116 cells and VERO was determined by MTT assay according to literature

protocols. Then, the absorbance of each well at 575 nm was determined by a Thermo Scientific Multiskan MK3 ELISA reader (Thermo Scientific, Waltham, MA). Five parallel wells were analyzed for each sample to get the mean cell viability value and the standard deviation [49–51].

Cellular uptake study

HCT116 cells were seeded on a coverslip in a 6-well plate at 0.3×10^6 cells per well, followed by treatment with free Rh and Rh-NPs, Rh-CS-NPs, and Rh-CS-FU-NPs. After 4 h of incubation at 37 ºC and 5% CO_2, cells were washed with PBS and fixed with 4% paraformaldehyde solution in PBS for 15 min. For antigen retrieval, cells were treated with Triton X for 5 min. Further, the background was blocked with 3% BSA solution treatment for 1 h. Washing was followed by incubation with FITC-tagged secondary antibody for 1 h at room temperature to observe the cytoskeleton details of the cells. Further, cells were washed with TBST 3 times, and counterstaining was done using 4', 6-diamidino-2-phenylindole (DAPI). Cells were observed using confocal laser scanning microscopy [52].

Assessment of ROS generation

The analysis method for ROS generation was the same as that reported previously [53]. HCT116 cells (2×10^5 cells/well) were seeded into 96-well plates. After cell adhesion, the cells were co-cultured with IC_{50} concentration of SOR-CS-FU-NPs, SOR-NPs, and free SOR for 24 h. The cells were incubated with 100 µL of 2, 7-dichlorofluorescein diacetate (DCFH-DA) probe in the dark for 30 min, and a cell imaging multimode reader (excitation wavelength: 488 nm; emission wavelength: 525 nm) was used to read the wavelength [53].

Mitochondrial membrane potential analysis

JC-1 is a lipophilic cationic dye that enters and aggregates inside the mitochondria, emitting red fluorescence. When mitochondrial membrane potential decreases, JC-1 no longer accumulates within mitochondria, resulting in green fluorescence. Briefly, HCT116 cells were seeded in a 6-well plate at a density of 2×10^5 cells per well and incubated

overnight. The IC_{50} concentration of SOR-CS-FU-NPs, SOR-NPs, and free SOR was added to the cells in DMEM containing 10% FBS and incubated for 24 h at 37 ºC. Cells were then washed three times with PBS buffer. After different treatments, cells were collected, centrifuged, and incubated with 500 µL of JC-1 for 20 minutes at 37 ºC. Cells without any treatment were used as controls [54].

Apoptosis by AO/EB staining

HCT116 cells were seeded in a 6-well plate at a density of 2×10^5 cells per well and incubated overnight. The IC_{50} concentration of SOR-CS-FU-NPs, SOR-NPs, and free SOR was added to the cells in DMEM containing 10% FBS and incubated for 24 h at 37 ºC. Cells were then washed three times with PBS buffer. After different treatments, cells were collected, centrifuged, and incubated with 5 µg/ml of AO/EB for 20 minutes at 37 ºC. Cells without any treatment were used as controls. After treatments, the cells were stained with AO/EB for 30 minutes and visualized under fluorescence microscopy [55–57].

Wound-healing assay

HCT116 cells were seeded in a 6-well plate at a density of 2×10^5 cells per well and incubated overnight, and the cells in DMEM containing 10% FBS were incubated for 24 h at 37 ºC. After 24 h, the artificial wound was created by a scratch method using a micropipette tip (200 µL) and washed with PBS to remove the cell debris. When the cells reached a confluent state, cells were scraped by a pipette tip at 4 h after adding IC_{50} concentration of SOR-CS-FU-NPs, SOR-NPs, and free SOR. Following treatments, the cells were visualized under fluorescence microscopy. The wound widths were measured [26].

Statistical analysis

Students' t-tests were used to assess the significance levels. n.s. signified not significance; *$p < 0.05$ represented statistical significance; **$p < 0.01$ indicated moderate statistical significance and ***$p < 0.001$ denoted highly statistical significance.

Results and discussion

Fabrication and characterization of SOR-NPs

The drug-loaded NPs were stabilized by fabricating SOR-NPs using nanoprecipitation and screening several surfactants. **Figure 2A** shows that out of Tween 80 surfactants, Pluronic F127, TPGS, PVA, and Tween 80 had the smallest diameter (123.10 ± 3.24 nm) and the best tolerable PDI (0.265 ± 0.039). In addition, we tested varying doses of the specified surfactant that affected the properties of the NPs. **Figure 2B** shows that the size of the NP and the PDI was inversely related to the concentration of Tween 80. During the preparation process, the surface of the NPs is coated with Tween 80, a non-ionic hydrophilic surfactant. Fewer particle interactions or fusions were shown as the concentration of this surfactant was increased, leading to an increase in the number of surfactant molecules on the surface of the NP. After further optimization trials, it was found that 1% Tween 80 produced the smallest particles with the lowest PDI.

Four different solvent-to-antisolvent ratios were tested further to investigate the effect on mean particle diameter and PDI [58]. The antisolvent phase (water phase) must have a higher volume to reduce NP size. The dispersion of NPs in a large surrounding aqueous phase minimizes the likelihood of particle aggregation in bigger quantities of liquid. The NPs with the smallest diameter (73.51 ± 1.69 nm) and PDI (0.114 ± 0.020) were obtained at a 1:3 solvent/antisolvent rate, as shown in **Figure 2C**, and were chosen for further optimization. After that, the optimal concentration of the polymer was determined to encapsulate a specific quantity of the drugs. The reduced ability of the polymer concentration to retain drug molecules resulted in increased average diameter and PDI with a drug-to-polymer ratio of 1:5. **Figure 2D** shows that particles with a low PDI and a smaller size were developed using a 1:10 drug-to-polymer ratio. The amount of polymer needed to entrap the maximal amount of drugs and keep the NPs stable in the suspension may be the reason for this subsequent drop. Increasing the polymer concentration led to greater polymer adsorption on the surface of the NP, which in turn caused the NPs to expand in size.

Figure 2E shows the results of loading an increasing SOR into the chosen polymer amount and solvent: antisolvent rate. Diameter and PDI were found to be small up to a loading of 0.17 mg/ml SOR; however, when the loading was more than 0.17 mg/ml, the size and PDI values increased. At a drug concentration of 0.17 mg/ml, the highest entrapment was 83.22%±3.31%, and this percentage rose as the drug amount increased (**Figure 2F**). The enhanced ability of the PLGA matrix to entrap SOR up to 0.17 mg/ml was demonstrated. In addition, EE decreased (45.94 ± 6.21%) when the drug concentration was increased by 0.18 mg/ml in the polymers rate. This may be because, at this SOR concentration, the NPs are already saturated with the drug molecule, and there is no longer any space for integrating more drug molecules. The optimal drug loading was thus determined to be 0.17 mg/ml.

The free amino groups' protonation on the polymer chain gives CS its positively charged nature. The positive charge on CS was attracted to the negative charge on PLGA, resulting in a coating of CS on SOR-NPs. In line with the earlier data, the SOR-NPs increased from negative (caused by PLGA-ester or carboxylic groups) to positive (caused by CS protonation of amino groups). **Figure 3A** shows a strong correlation between the increase in zeta potential and the rise in CS concentration. **Figure 3B** shows that an ideal zeta potential of 29.24 ± 3.74 mV, diameter, and PDI were achieved using a 0.5% CS. The second layer of CS was coated using electrostatic attraction and various concentrations of FU. Because it contains sulfate groups, FU has a negative charge. **Figure 3C** shows that incubation with increasing concentrations of FU lowered the zeta potential of SOR-CS-NPs, which are NPs coated with 0.5% CS. Increases in the coating concentration ratio of CS relative to FU resulted in SOR-CS-FU-NPs with positive zeta potential. **Figure 3D** shows that the mean NP size increased as the FU concentration increased. In the instance of a FU concentration of 0.1% w/v, there was a notable drop in zeta potential, measuring 18.23 ± 2.67 mV. Hence, the ideal concentration for coating the FU layer was determined to be 0.1% w/v FU. According to studies, CS is commonly utilized to develop functionalized nanocarriers because of its cationic character. In this study, CS was used to coat SOR-NPs with FU effectively.

Characterization of nanoparticles

The results for SOR formulations with various coating phases, including mean particle diameter, zeta potential, PDI, and drug loading percentage. **Figures 4A-4C** show the dynamic light scattering study outcomes for SOR-CS-NPs, SOR-FU NPs, and SOR-NPs. Findings showed that as coating thickness increased, both mean particle size and PDI also increased. SOR-NPs formed spherical particles devoid of aggregates, according to a transmission electron microscopy (TEM) study (**Figures 4D-4F**). **Figures 4D-4F** show that TEM images clearly showed that SOR-NPs were coated with a monolayer of CS. SOR-CS-NPs have a thin FU second layer coating, as shown in **Figures 4D-4F**. Additionally, FTIR analysis confirmed the presence of the thinly coated FU layer on top of the CS layer [59]. Additionally, after being incubated in serum for 12 h, SOR-CS-FU-NPs did not exhibit any notable variations in average particle diameter and PDI, proving stable in serum (**Figure 5A**). The SOR trapped in the nanoparticles was determined by DSC analysis. Thermogravimetric analyses of mannitol SOR-CS-FU-NP and free SOR are displayed in **Figure 5B**. A sharp peak occurred at 270-285 °C for SOR, a crystalline API. However, SOR found no evidence of this endothermic peak characteristic in the SOR-CS-FU NP. This proved that the SOR is not precipitated but exists in an amorphous form within the nanoparticle surface. As a cryoprotectant, mannitol is responsible for the other steep band shown in the formulation between 165 and 167 °C when lyophilized. **Figure 5C** shows the PXRD profile of mannitol, free SOR, and SOR-CS-FU NP. The PXRD showed the crystalline structure of mannitol and free SOR, which exhibited crisp and strong peaks. There was a considerable ratio of amorphous form without the essential bands of SOR and a noticeable loss in crystallinity in the lyophilized form of the developed SOR-CS-FU NP formulation. These findings prove that the SOR is an amorphous form trapped inside the NP.

Figure 5D displays the FTIR spectra acquired for the free SOR, Blank-NPs, SOR-NPs, SOR-CS-NPs, and SOR-CS-FU-NPs. The SOR spectra showed distinct absorption peaks at 1612 cm^{-1} for C=O groups, 2824 cm^{-1} for methylene C-H groups, 2954 cm^{-1} for CH_3 groups, 3207 cm^{-1} for O-H groups, and 3455 cm^{-1} for N-H groups. The blank-PLGA-NPs

showed peaks at 1085 and 1175 cm^{-1}, corresponding to the ether groups focused at 1753 cm-1, responsible for a noticeable resonance. The PLGA-NPs were associated with resonances at 1451, 2995, 2947, and cm^{-1}, which were determined to be CH, CH_2, and CH_3 stretching vibrations. The surface functional groups of SOR-NPs have chemical characteristics identical to those of PLGA and SOR, according to the spectral study of these NPs. The FTIR spectra did not reveal chemical interactions between the SOR functional groups and the polymer. The presence of drug peaks in the formulation of the nanoparticles indicated that the surface contained some free drugs. A prominent band indicated O-H and N-H bonds and hydrogen bonds stretching in pure CS in the 3352-3287 cm^{-1} region. The asymmetric stretching of C-H bonds is responsible for the absorption bands observed at around 2865 cm^{-1}. Glucosidic C-O-C, C-H, and C=O and amide I groups were further suggested by 1647, 1373, and 893 cm-1 bands, respectively. Two strong bands at 1542 and 1631 cm^{-1} correspond to the movement of amide and amine bonds, and the amide bands of CS at 3207 cm^{-1} indicated the adsorption of CS on the surface in the spectra of SOR-CS-NPs. In addition, at 1751 cm^{-1}, a little signal indicated the presence of PLGA. Additionally, FU showed a wide range of spectra at 3425-3410 cm^{-1} because of the O-H and distinct bands at 2985 and 2934 cm^{-1} for the C-H of the fucose methyl group and pyranose ring, respectively. SOR-CS-FU-NPs showed the classic CS and FU peaks. The intermolecular interaction, which could have occurred through the electrostatic interaction and hydrogen bond formation between the positive charge CS amino groups and the negative charge FU sulfate groups, was confirmed by a redshift from 1655 to 1630 cm^{-1}, which showed a change in the amide band [60–62]. It was confirmed by the observed FTIR spectra that SOR-CS-NPs were coated with FU. The atomic force microscopy (AFM) analysis image studied the size and surface morphology of the fabricated SOR-CS-FU-NPs (**Figure 5E)**. The attained AFM image revealed that the fabricated SOR-CS-FU-NPs were spherical without other observable nanostructure morphologies established by the absorbance spectrum. The particles were not greatly mono-dispersed but seemed non-agglomerated. This is because some essential capping agents, fucoidan (FU) and chitosan, efficiently stabilize the fabricated SOR-CS-FU-NPs.

In-vitro drug release studies

Figure 6A shows the results of in vitro drug release experiments using optimized SOR-CS-FU-NPs, regular SOR-NPs, free SOR solution, and SOR CS-NPs. Investigation indicates that SOR was released from various NPs and that it was compared to a free SOR suspension. SOR-CS-FU-NPs, SOR-CS-NPs, and SOR-NP exhibited a quick release of approximately 25-35% in the first 6 h, followed by steady release behaviour for up to 120 h. SOR-CS-FU-NPs (76.67 ± 0.027%) and SOR-CS-NPs (81.36 ± 0.980%) had lower cumulative SOR release rates than SOR-NPs (88.64 ± 2.375%). As a barrier, the CS and FU multilayer coating on the PLGA NPs may regulate the SOR's diffusion (**Figure 6B**). This may explain whether SOR-CS-FU-NPs and SOR-CS-NPs have a prolonged release.

The data obtained from the dialysis release study was analyzed using various kinetic models, including the Zero order kinetic model, the First order kinetic model, the Higuchi model, and the Korsmeyer–Peppas model. The results of the Zero order kinetic model, the First order kinetic model, the Higuchi model, and the Korsmeyer-Peppas model were 0.8649, 0.9402, 0.9699, and 0.434, respectively. The analysis revealed that Higuchi's equation provided the most precise rationale for the in vitro SOR release from SOR-CS-FU-NPs, as indicated by the highest regression value, indicating the most vital linear connection. The slower rate of drug diffusion is attributed to the increase in distance for diffusion, which follows either square root kinetics or Higuchi kinetics. The diffusion exponent (n) derived from applying the Korsmeyer-Peppas kinetics model was less than 0.45 (n=0.434). This result indicates that the release mechanism follows Fickian diffusion [63].

Cytotoxicity assay

Figure 7A shows that the cytotoxicity of free SOR, SOR-NPs, and SOR-CS-FU-NPs varied with concentration. The SOR-CS-FU-NPs treated group exhibited significantly greater cytotoxicity across all concentrations than free SOR. The in vitro effectiveness of each group against colon cancer was also evaluated by calculating their IC_{50}. Compared to free SOR (IC_{50} 157.05 µg/ml), the IC_{50} value of 19.61 µg/ml for SOR-CS-FU-NPs is 8.0 times

lower. The IC_{50} value of SOR-NPs was 35.05 µg/ml, 1.8 times lower than free SOR. The developed SOR-CS-FU-NPs may have a reduced IC_{50} value because FU interacts with HCT116 cells, which improves cellular uptake [64].

In addition, the toxicity ability of the new formulation was evaluated by conducting a cytotoxicity assessment for NPs in a non-cancer VERO cell line. With a maximum of 25% cell inhibition, shown tested concentrations of Blank-NPs, SOR-CS-FU-NPs, and SOR-NPs, the testing results demonstrated that the developed NPs are harmless. SOR-CS-FU-NPs inhibited cell concentration-independent (**Figure 7B**), showing their safety for use with healthy cells. Because of the biocompatibility of the formulation comprising PLGA, CS, and FU, the developed SOR-CS-FU-NPs were discovered to be less cytotoxic and safe in VERO cell lines. In addition, increasing the concentration of free SOR from 5 to 80 µg/ml did not significantly affect cell survival. In keeping with earlier findings published by Gilani et al., the non-cancer VERO cell line showed an effect of free SOR therapy. When comparing SOR and HCT116, they found that non-cancer VERO cell line cells were more resistant to SOR's anticancer effects. Furthermore, although non-cancer cells have relatively low expression of Src-kinase protein, cancer cells like the HCT116 cell line have remarkably overexpressed Src-kinase, resulting in a greater activity of SOR in HCT116.

Cellular uptake study

Figure 8 shows the results of the qualitative study comparing the cell uptake of Rh-loaded nanoformulations to that of Rh alone. It exhibited a solid red fluorescence compared to free Rh, Rh-NPs, Rh-CS-NPs, and Rh-CS-FU-NPs. Due to the positive surface charge and receptor-mediated endocytosis on nanoparticles, this finding suggested that Rh-CS-FU-NPs were more effectively internalized by the cells. **Figure 8A** shows that compared to Rh-CS-NPs, Rh-FU-CS-NPs exhibited 3.09 times more absorption in HCT116 cells. Based on the results, active targeting is crucial for enhancing NP absorption into cancer cells via interactions between FU, positively charged surfaces, and activated P-selectin receptors. Previous research finds a good match with the FU-mediated increased uptake [65]. In addition, compared to free Rh, the cellular absorption of Rh-CS-FU-NPs was 19.0 times

more, according to the quantitative study (**Figure 8B**). The enhanced cellular uptake of SOR-CS-FU-NPs is directly related to their increased cytotoxicity potential compared to free SOR.

Assessment of ROS generation

The fluorescent dye DCFH-DA staining was employed to evaluate ROS generation in cancer cells using NPs [66]. DCFH-DA does not glow when it is outside of cells. When esterase reaches the cell, it splits DCFH-DA into DCFH. Additionally, the produced ROS oxidizes DCFH to DCF, which possesses luminous characteristics. We measured the fluorescence of the cells treated with NPs and reported the ROS formation as ROS level (% of untreated). **Figure 9A** shows that compared to free SOR (167.20 ± 29.95 % of untreated), ROS production was much higher in SOR-CS-FU-NPs (572.33 ± 42.19 % of untreated). Afterwards, compared to free SOR, ROS generation was much greater in SOR-NPs (380.02 ± 45.60% of untreated). According to these findings, both SOR-CS-FU-NPs and SOR-NPs caused HCT116 cells to produce ROS inside their cells. In addition, these results may be associated with NPs causing more cell death. When compared to free SOR, ROS-mediated cytotoxicity is significantly higher. One possible explanation for the observed rise in ROS levels is the increased internalization of SOR-CS-FU-NPs (**Figure 9B**). Ensuring survival depends on redox homeostasis and cell proliferation. When anticancer drugs raise ROS levels, they delay signalling process timing. Increased cell death was also associated with increased uptake of active NPs through specific delivery systems.

Mitochondrial membrane potential (MMP) analysis

The change in fluorescence from red to green, as measured by the fluorescent cationic dye JC-1, was used to quantify the potential disruption of the mitochondrial membrane [67]. Red fluorescence in live cell lines is produced by interacting with the mitochondrial membrane, and green fluorescence is produced when MMP is reduced. The negative charge developed by the exact MMP allows the JC-1 staining to enter the mitochondria in healthy cells, forming an aggregation (red fluorescence). Since the mitochondrial

membrane potential is lost in apoptosis cell lines, the JC-1 staining builds up in the monomeric form of cytoplasm (green fluorescence). After being treated for 48 h, both SOR and SOR-NPs showed malfunction of membrane potential, as shown in **Figure 10A**. Green fluorescence was substantially higher in the SOR-CS-FU-NPs group compared to the free SOR group. Additionally, as compared to SOR-NPs, it exhibited significantly more green fluorescence. After treatment with NPs, the combined fluorescence pictures shifted from red to yellow, as shown in fluorescent photomicrographs (**Figure 10B**). The results of flow cytometry analysis showed that JC-1 was more concentrated in the cytoplasm after HCT116 cells were treated with NPs. This suggests the mitochondrial membrane was more depolarized than when cells were treated with free SOR (**Figure 10C**). Damage to mitochondria is a direct result of reactive oxygen species (ROS) generated within cells. The activation of the mitochondrial-mediated apoptotic pathway was indicated by the elevation of ROS levels in cells treated with SOR-CS-FU-NPs and SOR-NPs (**Figure 10D**).

Apoptosis assay

Nuclear variations and apoptosis in HCT116 cells were detected by acridine orange/ethidium bromide labelling [68–70]. Green fluorescence was observed in non-apoptotic and living cells, while red fluorescence was observed in apoptotic cells. When comparing cells treated with free SOR to those treated with SOR-CS-FU-NPs, the nucleus of the former exhibits more red fluorescence (**Figure 11A**). The experimental group that received SOR-NPs also showed more red fluorescence than those that received free SOR. Nuclear morphology also changed in the SOR-CS-FU NP group compared to the others. Undifferentiated nucleus outlining increase in cell volume. Also, these cells showed signs of disintegration by emitting an uneven reddish colour (**Figure 11B**). Based on these findings, it appears that FU-tailored SOR-NPs induce necrosis in HCT116 cells. Cells treated with SOR-NPs exhibited signs of cell disintegration earlier than cells treated with free SOR, indicating a higher rate of apoptotic cell death. Further, the apoptosis mechanism was confirmed by the Annexin V-FITC and PI staining by flow cytometry analysis. The results of flow cytometry analysis revealed that the fabricated SOR-CS-FU-NPs induce high ratio apoptosis based on the results shown in **Figures 11C and 11D**.

Figure 10 highlights that the apoptosis index of SOR-CS-FU-NPs was 7.5 times greater than free SOR. One possible explanation for the SOR-CS-FU-NPs' greater cell-killing ability is that they induce apoptosis through intrinsic pathways and are more absorbed by cells. The results of the apoptosis assays employing the JC-1 dye and DCFH-DA assay were validated by the elevated ROS generation and mitochondrial membrane potential disruption caused by SOR-CS-FU-NPs. Increased reactive oxygen species (ROS) and oxidative stress caused lipid peroxidation and denaturation of proteins, which damaged cell membranes. Necrosis and DNA damage caused cell death as a result of this process.

Wound-healing assay

There is an increase in mortality rates due to the greater probability of metastatic behaviour in colon cancer cells [71]. The ability of HCT116 cells to migrate is strong. Anticancer drugs' antineoplastic activity is typically demonstrated using the scratch assay. We used a wound-healing or scratch experiment to determine whether the developed NPs may restrict cell mobility, as shown in **Figure 12A**. Out of all the groups, the untreated group had the highest rate of wound closure at 73.10 ± 2.03%. As for the wound closure, percentages were 52.96 ± 2.31% for free SOR, 22.24 ± 8.33% for SOR-NPs, and 5.04 ± 2.08% for SOR-CS-FU-NPs. Compared to the untreated group, HCT116 cells treated with free SOR had a much-reduced ability to heal (**Figure 12B**). Nevertheless, compared to the free SOR group, SOR-CS-FU-NPs and SOR-NPs showed a substantially reduced percentage of wound closure. Compared to SOR-NPs, SOR-CS-FU-NPs showed fewer wound-closing properties. Therefore, due to their excellent absorption in HCT116 cells, SOR-CS-FU-NPs demonstrated outstanding metastatic circumvention potential in wound-healing results.

Conclusion

In this study, the sorafenib-loaded fucoidan and chitosan nanoparticles showed strong anticancer activity and controlled release under simulated gastrointestinal environments. FU was chosen as a targeting ligand because of the high levels of P-selectin expression

in colon cancer cells. The composition of FU-anchored PLGA NPs carrying SOR was thoroughly adjusted to achieve the necessary particle size and encapsulation efficiency. The process of attaching FU to PLGA NPs was carried out successfully, resulting in the active targeting of colon cancer cells. The formulated solution exhibited a high level of biocompatibility, resulting in a considerable reduction in hemotoxicity. Furthermore, the SOR-CS-FU nanoparticles exhibited a significantly delayed drug release. This characteristic will be beneficial in dropping the frequency of drug administration, thereby diminishing adverse effects. The nanoparticles demonstrated a significant rise in cellular uptake and enhanced apoptotic efficacy. The coated formulation demonstrated a much lower IC_{50} and an impaired mitochondrial potential, which supports its targeting efficiency. Therefore, adjusting the diameter of the particles and modifying their surface with FU could be a favourable strategy for controlling colon cancer cells by enhancing programmed cell death and toxicity.

Funding

The present study was supported by the Found of the Suzhou Science and Technology Development Project (NO. SKY2022191).

Author information:

Authors and Affiliations

Yu Zhou, Xiaodong Yang, Chungen Xing

Department of General Surgery, The Second Affiliated Hospital of Soochow University, Suzhou 215000, Jiangsu Province, China.

Wen Lu, Tingjun Wang, Chunrong Sun

Department of General Surgery, The Affiliated Suzhou Hospital of Nanjing Medical University, Suzhou Municipal Hospital, Gusu School, Nanjing Medical University, Suzhou 215000, Jiangsu Province, China.

Jin Liu

Department of Infectious Diseases, The Affiliated Infectious Diseases Hospital, Suzhou Medical College of Soochow University, The Fifth Hospital of Suzhou, Suzhou 215000, Jiangsu Province, China.

Sai Ma

Department of Central Laboratory, The Affiliated Suzhou Hospital of Nanjing Medical University, Suzhou Municipal Hospital, Gusu School, Nanjing Medical University, Suzhou 215000, Jiangsu Province, China.

Zhenzhen Zou

Department of Laboratory, The Fourth Affiliated Hospital of Soochow University, Dushuhu Public Hospital Affiliated to Soochow University, Suzhou 215000, Jiangsu Province, China.

Contributions:

Yu Zhou, Jin Liu: Conceptualization, Writing, Data curation, Software, Writing Original Draft, and Methodology. **Sai Ma, Xiaodong Yang, Zhenzhen Zou:** Analyzed and Interpreted the Data, Resources, Contributed Reagents and Materials. **Wen Lu, Tingjun Wang, Chunrong Sun:** Analysis data, and Software. **Chunrong Sun and Chungen Xing:** Conceptualization, Project Administration, and Writing - Review & Editing.

Corresponding authors

Correspondence to **Dr. Chungen Xing and Dr. Chunrong Sun**

Competing interests:

The authors declare that they have no competing interests.

Ethical approval:

Not applicable.

Consent for publication:

Not applicable.

Data availability statement

The data supporting this study's findings are available from the corresponding author upon reasonable request.

References

[1] R. Mata, J.R. Nakkala, S.R. Sadras, Therapeutic role of biogenic silver and gold nanoparticles against a DMH-induced colon cancer model, Biomater. Adv. 146 (2023) 213279.

[2] R. You, J. Li, H. Wang, Y. Wu, J. Weng, Y. Lu, High-performance SERS biosensor based on in-situ reduction of silver nanoparticles in an ultra-filtration centrifuge device for label-free detection of colon cancer in serum, J. Memb. Sci. 678 (2023) 121688.

[3] G. Shafiei, D. Jafari-Gharabaghlou, M. Farhoudi-Sefidan-Jadid, E. Alizadeh, M. Fathi, N. Zarghami, Targeted delivery of silibinin via magnetic niosomal nanoparticles: potential

application in treatment of colon cancer cells, Front. Pharmacol. 14 (2023) 1174120.
[4] H. Yuan, H. Gui, S. Chen, L. Zhu, C. Wang, Q. Jing, H. Lv, Q. Wan, S. Wang, S. Zhou, Regulating tumor-associated macrophage polarization by cyclodextrin-modified PLGA nanoparticles loaded with R848 for treating colon cancer, Int. J. Nanomedicine. (2024) 3589–3605.
[5] R. Garg, M. Gaur, B.G. Prajapati, G. Agrawal, S. Bhattacharya, G.M. Elossaily, Polymeric nanoparticles approach and identification and characterization of novel biomarkers for colon cancer, Results Chem. 6 (2023) 101167.
[6] A. Dey, A. Mitra, S. Pathak, S. Prasad, A.S. Zhang, H. Zhang, X.-F. Sun, A. Banerjee, Recent advancements, limitations, and future perspectives of the use of personalized medicine in treatment of colon cancer, Technol. Cancer Res. Treat. 22 (2023) 15330338231178404.
[7] K.E. Cox, S. Liu, T.M. Lwin, R.M. Hoffman, S.K. Batra, M. Bouvet, The mucin family of proteins: candidates as potential biomarkers for colon cancer, Cancers (Basel). 15 (2023) 1491.
[8] B.F. Far, M.R. Naimi-Jamal, H. Daneshgar, N. Rabiee, Co-delivery of doxorubicin/sorafenib by DNA-decorated green ZIF-67-based nanocarriers for chemotherapy and hepatocellular carcinoma treatment, Environ. Res. 225 (2023) 115589.
[9] A. Carmignani, M. Battaglini, A. Marino, F. Pignatelli, G. Ciofani, Drug-Loaded Polydopamine Nanoparticles for Chemo/Photothermal Therapy against Colorectal Cancer Cells, ACS Appl. Bio Mater. 7 (2024) 2205–2217.
[10] Y. Yu, X. Shen, X. Xiao, L. Li, Y. Huang, Butyrate modification promotes intestinal absorption and hepatic cancer cells targeting of ferroptosis inducer loaded nanoparticle for enhanced hepatocellular carcinoma therapy, Small. 19 (2023) 2301149.
[11] Y. Xu, L. Yang, C. Wang, W. Sun, Y. Zheng, B. Ou, L. Wu, L. Shi, X. Lin, W. Chen, Ferroptosis boosted oral cancer photodynamic therapy by carrier-free Sorafenib-Ce6 self-assembly nanoparticles, J. Control. Release. 366 (2024) 798–811.
[12] M. Dahiya, R. Awasthi, K. Dua, H. Dureja, Sorafenib tosylate loaded superparamagnetic nanoparticles: Development, optimization and cytotoxicity analysis on HepG2 human hepatocellular carcinoma cell line, J. Drug Deliv. Sci. Technol. 79 (2023) 104044.
[13] H. Tian, T. Zhang, S. Qin, Z. Huang, L. Zhou, J. Shi, E.C. Nice, N. Xie, C. Huang, Z. Shen, Enhancing the therapeutic efficacy of nanoparticles for cancer treatment using versatile targeted strategies, J. Hematol. Oncol. 15 (2022) 132. https://doi.org/10.1186/s13045-022-01320-5.
[14] X. Huang, W. Wu, W. Yang, X. Qing, Z. Shao, Surface engineering of nanoparticles with

ligands for targeted delivery to osteosarcoma, Colloids Surfaces B Biointerfaces. 190 (2020) 110891. https://doi.org/https://doi.org/10.1016/j.colsurfb.2020.110891.

[15] S. Indoria, V. Singh, M.-F. Hsieh, Recent advances in theranostic polymeric nanoparticles for cancer treatment: A review, Int. J. Pharm. 582 (2020) 119314.

[16] M. Alsehli, Polymeric nanocarriers as stimuli-responsive systems for targeted tumor (cancer) therapy: Recent advances in drug delivery, Saudi Pharm. J. 28 (2020) 255–265.

[17] N. Avramović, B. Mandić, A. Savić-Radojević, T. Simić, Polymeric nanocarriers of drug delivery systems in cancer therapy, Pharmaceutics. 12 (2020) 298.

[18] H. Jin, T. Zhu, X. Huang, M. Sun, H. Li, X. Zhu, M. Liu, Y. Xie, W. Huang, D. Yan, ROS-responsive nanoparticles based on amphiphilic hyperbranched polyphosphoester for drug delivery: Light-triggered size-reducing and enhanced tumor penetration, Biomaterials. 211 (2019) 68–80. https://doi.org/https://doi.org/10.1016/j.biomaterials.2019.04.029.

[19] V. Ejigah, O. Owoseni, P. Bataille-Backer, O.D. Ogundipe, F.A. Fisusi, S.K. Adesina, Approaches to improve macromolecule and nanoparticle accumulation in the tumor microenvironment by the enhanced permeability and retention effect, Polymers (Basel). 14 (2022) 2601.

[20] M. Sheydaei, E. Alinia-Ahandani, Cancer and polymeric-carriers, Biomed J Sci Tech Res. 31 (2020) 24107–24110.

[21] P.K. Gupta, R. Gahtori, K. Govarthanan, V. Sharma, S. Pappuru, S. Pandit, A.S. Mathuriya, S. Dholpuria, D.K. Bishi, Recent trends in biodegradable polyester nanomaterials for cancer therapy, Mater. Sci. Eng. C. 127 (2021) 112198.

[22] M. Su, S. Xiao, M. Shu, Y. Lu, Q. Zeng, J. Xie, Z. Jiang, J. Liu, Enzymatic multifunctional biodegradable polymers for pH-and ROS-responsive anticancer drug delivery, Colloids Surfaces B Biointerfaces. 193 (2020) 111067.

[23] W. Xia, Z. Tao, B. Zhu, W. Zhang, C. Liu, S. Chen, M. Song, Targeted delivery of drugs and genes using polymer nanocarriers for cancer therapy, Int. J. Mol. Sci. 22 (2021) 9118.

[24] K.H. Wong, A. Lu, X. Chen, Z. Yang, Natural ingredient-based polymeric nanoparticles for cancer treatment, Molecules. 25 (2020) 3620.

[25] M.M. Yallapu, B.K. Gupta, M. Jaggi, S.C. Chauhan, Fabrication of curcumin encapsulated PLGA nanoparticles for improved therapeutic effects in metastatic cancer cells, J. Colloid Interface Sci. 351 (2010) 19–29.

[26] L. Baghirova, E. Kaya Tilki, A.A. Öztürk, Evaluation of Cell Proliferation and Wound

671 Healing Effects of Vitamin A Palmitate-Loaded PLGA/Chitosan-Coated PLGA Nanoparticles:
672 Preparation, Characterization, Release, and Release Kinetics, ACS Omega. 8 (2023) 2658–2668.
673 https://doi.org/10.1021/acsomega.2c07232.
674 [27] W. Lin, C. Li, N. Xu, M. Watanabe, R. Xue, A. Xu, M. Araki, R. Sun, C. Liu, Y. Nasu, Dual-
675 functional PLGA nanoparticles co-loaded with indocyanine green and resiquimod for prostate
676 cancer treatment, Int. J. Nanomedicine. 16 (2021) 2775.
677 [28] Y. Lin, X. Qi, H. Liu, K. Xue, S. Xu, Z. Tian, The anticancer effects of fucoidan: A review of
678 both in vivo and in vitro investigations, Cancer Cell Int. 20 (2020) 154.
679 [29] Y. Lu, Q. Pan, W. Gao, Y. Pu, K. Luo, B. He, Z. Gu, Leveraging disulfiram to treat cancer:
680 Mechanisms of action, delivery strategies, and treatment regimens, Biomaterials. 281 (2022)
681 121335. https://doi.org/https://doi.org/10.1016/j.biomaterials.2021.121335.
682 [30] C.-H. Chung, K.-Y. Lu, W.-C. Lee, W.-J. Hsu, W.-F. Lee, J.-Z. Dai, P.-W. Shueng, C.-W.
683 Lin, F.-L. Mi, Fucoidan-based, tumor-activated nanoplatform for overcoming hypoxia and
684 enhancing photodynamic therapy and antitumor immunity, Biomaterials. 257 (2020) 120227.
685 https://doi.org/https://doi.org/10.1016/j.biomaterials.2020.120227.
686 [31] Z. Zhao, F. Yang, X. Zhang, J. Sun, Z. He, C. Luo, Emerging nanotherapeutics for
687 antithrombotic treatment, Biomaterials. 255 (2020) 120200.
688 https://doi.org/https://doi.org/10.1016/j.biomaterials.2020.120200.
689 [32] H. Wang, R. Hunter, Q. Zhang, H. Yu, J. Wang, Y. Yue, L. Geng, N. Wu, The application of
690 marine polysaccharides to antitumor nanocarriers, Carbohydr. Polym. 342 (2024) 122407.
691 https://doi.org/https://doi.org/10.1016/j.carbpol.2024.122407.
692 [33] V. Dulong, P. Thebault, C. Karakasyan, L. Picton, D. le Cerf, Polyelectrolyte complexes of
693 chitosan and hyaluronic acid or carboxymethylpullulan and their aminoguaiacol derivatives with
694 biological activities as potential drug delivery systems, Carbohydr. Polym. 341 (2024) 122330.
695 https://doi.org/https://doi.org/10.1016/j.carbpol.2024.122330.
696 [34] S.M. Etman, Y.S.R. Elnaggar, O.Y. Abdallah, Fucoidan, a natural biopolymer in cancer
697 combating: From edible algae to nanocarrier tailoring, Int. J. Biol. Macromol. 147 (2020) 799–
698 808.
699 [35] B. Mabate, C.D. Daub, S. Malgas, A.L. Edkins, B.I. Pletschke, Fucoidan structure and its
700 impact on glucose metabolism: Implications for diabetes and cancer therapy, Mar. Drugs. 19
701 (2021) 30.
702 [36] C.C.F. Do-Amaral, B.S. Pacheco, F.K. Seixas, C.M.P. Pereira, T. Collares, Antitumoral

effects of fucoidan on bladder cancer, Algal Res. 47 (2020) 101884.
[37] Y. Fu, H. Jiao, J. Sun, C.O. Okoye, H. Zhang, Y. Li, X. Lu, Q. Wang, J. Liu, Structure-activity relationships of bioactive polysaccharides extracted from macroalgae towards biomedical application: A review, Carbohydr. Polym. 324 (2024) 121533. https://doi.org/https://doi.org/10.1016/j.carbpol.2023.121533.
[38] R.F.N. Quadrado, S. Silvestri, J.F. de Souza, B.A. Iglesias, A.R. Fajardo, Advances in porphyrins and chlorins associated with polysaccharides and polysaccharides-based materials for biomedical and pharmaceutical applications, Carbohydr. Polym. 334 (2024) 122017. https://doi.org/https://doi.org/10.1016/j.carbpol.2024.122017.
[39] G. Chen, L. Yu, F. Shi, J. Shen, Y. Zhang, G. Liu, X. Mei, X. Li, X. Xu, C. Xue, Y. Chang, A comprehensive review of sulfated fucan from sea cucumber: Antecedent and prospect, Carbohydr. Polym. 341 (2024) 122345. https://doi.org/https://doi.org/10.1016/j.carbpol.2024.122345.
[40] C.R. Corso, N. Mulinari Turin de Oliveira, L. Moura Cordeiro, K. Sauruk da Silva, S.H. da Silva Soczek, V. Frota Rossato, E.S. Fernandes, D. Maria-Ferreira, Polysaccharides with antitumor effect in breast cancer: a systematic review of non-clinical studies, Nutrients. 13 (2021) 2008.
[41] J.-O. Jin, D. Yadav, K. Madhwani, N. Puranik, V. Chavda, M. Song, Seaweeds in the Oncology Arena: Anticancer Potential of Fucoidan as a Drug—A Review, Molecules. 27 (2022) 6032.
[42] B. Pradhan, S. Patra, R. Nayak, C. Behera, S.R. Dash, S. Nayak, B.B. Sahu, S.K. Bhutia, M. Jena, Multifunctional role of fucoidan, sulfated polysaccharides in human health and disease: A journey under the sea in pursuit of potent therapeutic agents, Int. J. Biol. Macromol. 164 (2020) 4263–4278.
[43] T. Li, J. Yang, C. Weng, P. Liu, Y. Huang, S. Meng, R. Li, L. Yang, C. Chen, X. Gong, Intra-articular injection of anti-inflammatory peptide-loaded glycol chitosan/fucoidan nanogels to inhibit inflammation and attenuate osteoarthritis progression, Int. J. Biol. Macromol. 170 (2021) 469–478.
[44] G. Guillén, P. Montero García, Enhancement of oral bioavailability of natural compounds and probiotics by mucoadhesive tailored biopolymer-based nanoparticles: A review, (2021).
[45] N. Zahariev, P. Katsarov, P. Lukova, B. Pilicheva, Novel Fucoidan Pharmaceutical Formulations and Their Potential Application in Oncology—A Review, Polymers (Basel). 15

(2023) 3242.
[46] Y.A. Haggag, A.A. Abd Elrahman, R. Ulber, A. Zayed, Fucoidan in pharmaceutical formulations: a comprehensive review for smart drug delivery systems, Mar. Drugs. 21 (2023) 112.
[47] R. Yang, W.-S. Shim, F.-D. Cui, G. Cheng, X. Han, Q.-R. Jin, D.-D. Kim, S.-J. Chung, C.-K. Shim, Enhanced electrostatic interaction between chitosan-modified PLGA nanoparticle and tumor, Int. J. Pharm. 371 (2009) 142–147. https://doi.org/https://doi.org/10.1016/j.ijpharm.2008.12.007.
[48] S.-C. Chen, Y.-C. Wu, F.-L. Mi, Y.-H. Lin, L.-C. Yu, H.-W. Sung, A novel pH-sensitive hydrogel composed of N,O-carboxymethyl chitosan and alginate cross-linked by genipin for protein drug delivery, J. Control. Release. 96 (2004) 285–300. https://doi.org/https://doi.org/10.1016/j.jconrel.2004.02.002.
[49] L. Holden, C.S. Burke, D. Cullinane, T.E. Keyes, Strategies to promote permeation and vectorization, and reduce cytotoxicity of metal complex luminophores for bioimaging and intracellular sensing, RSC Chem. Biol. 2 (2021) 1021–1049. https://doi.org/10.1039/D1CB00049G.
[50] C. Yuan, B. Jiang, X. Xu, Y. Wan, L. Wang, J. Chen, Anti-human ovarian cancer and cytotoxicity effects of nickel nanoparticles green-synthesized by Alhagi maurorum leaf aqueous extract, J. Exp. Nanosci. 17 (2022) 113–125. https://doi.org/10.1080/17458080.2021.2011860.
[51] L.R. de Moura Ferraz, A.É.G.A. Tabosa, D.D.S. da Silva Nascimento, A.S. Ferreira, V. de Albuquerque Wanderley Sales, J.Y.R. Silva, S.A. Júnior, L.A. Rolim, J.J. de Souza Pereira, P.J. Rolim-Neto, ZIF-8 as a promising drug delivery system for benznidazole: development, characterization, in vitro dialysis release and cytotoxicity, Sci. Rep. 10 (2020) 16815. https://doi.org/10.1038/s41598-020-73848-w.
[52] Y. Huang, L. He, W. Liu, C. Fan, W. Zheng, Y.-S. Wong, T. Chen, Selective cellular uptake and induction of apoptosis of cancer-targeted selenium nanoparticles, Biomaterials. 34 (2013) 7106–7116. https://doi.org/https://doi.org/10.1016/j.biomaterials.2013.04.067.
[53] W. Zuo, D. Chen, Z. Fan, L. Chen, Z. Zhu, Q. Zhu, X. Zhu, Design of light/ROS cascade-responsive tumor-recognizing nanotheranostics for spatiotemporally controlled drug release in locoregional photo-chemotherapy, Acta Biomater. 111 (2020) 327–340. https://doi.org/https://doi.org/10.1016/j.actbio.2020.04.052.
[54] J. Singh, A. Dwivedi, L. Ray, D. Chopra, D. Dubey, A.K. Srivastva, S. Kumari, R.K. Yadav,

S.K. Amar, C. Haldar, R.S. Ray, PLGA nanoformulation of sparfloxacin enhanced antibacterial activity with photoprotective potential under ambient UV-R exposure, Int. J. Pharm. 541 (2018) 173–187. https://doi.org/https://doi.org/10.1016/j.ijpharm.2018.02.028.

[55] D. Albayrak, O. Doğanlar, S. Erdoğan, M. Meraklı, A. Doğan, P. Turker, A. Bostancı, Z.B. Doğanlar, Naringin Combined with NF-κB Inhibition and Endoplasmic Reticulum Stress Induces Apoptotic Cell Death via Oxidative Stress and the PERK/eIF2α/ATF4/CHOP Axis in HT29 Colon Cancer Cells, Biochem. Genet. 59 (2021) 159–184. https://doi.org/10.1007/s10528-020-09996-5.

[56] Y. Hu, D. Yu, X. Zhang, 9-amino acid cyclic peptide-decorated sorafenib polymeric nanoparticles for the efficient in vitro nursing care analysis of hepatocellular carcinoma, Process Biochem. 100 (2021) 140–148. https://doi.org/https://doi.org/10.1016/j.procbio.2020.09.021.

[57] S. Kasibhatla, G.P. Amarante-Mendes, D. Finucane, T. Brunner, E. Bossy-Wetzel, D.R. Green, Acridine Orange/Ethidium Bromide (AO/EB) Staining to Detect Apoptosis, CSH Protoc. 2006 (2006) 799–803. https://doi.org/10.1101/pdb.prot4493.

[58] I. Takeuchi, T. Suzuki, K. Makino, Skin permeability and transdermal delivery route of 50-nm indomethacin-loaded PLGA nanoparticles, Colloids Surfaces B Biointerfaces. 159 (2017) 312–317. https://doi.org/https://doi.org/10.1016/j.colsurfb.2017.08.003.

[59] J. Liu, Z. Qian, Q. Shi, S. Yang, Q. Wang, B. Liu, J. Xu, X. Guo, H. Liu, An asymmetric wettable chitosan–silk fibroin composite dressing with fixed silver nanoparticles for infected wound repair: in vitro and in vivo evaluation, RSC Adv. 7 (2017) 43909–43920. https://doi.org/10.1039/C7RA07588J.

[60] S. Yu, X. Zhang, G. Tan, L. Tian, D. Liu, Y. Liu, X. Yang, W. Pan, A novel pH-induced thermosensitive hydrogel composed of carboxymethyl chitosan and poloxamer cross-linked by glutaraldehyde for ophthalmic drug delivery, Carbohydr. Polym. 155 (2017) 208–217. https://doi.org/https://doi.org/10.1016/j.carbpol.2016.08.073.

[61] K. Saravanakumar, A.V.A. Mariadoss, A. Sathiyaseelan, K. Venkatachalam, X. Hu, M.-H. Wang, pH-sensitive release of fungal metabolites from chitosan nanoparticles for effective cytotoxicity in prostate cancer (PC3) cells, Process Biochem. 102 (2021) 165–172. https://doi.org/https://doi.org/10.1016/j.procbio.2020.12.005.

[62] C. Viezzer, R. Mazzuca, D.C. Machado, M.M. de Camargo Forte, J.L. Gómez Ribelles, A new waterborne chitosan-based polyurethane hydrogel as a vehicle to transplant bone marrow mesenchymal cells improved wound healing of ulcers in a diabetic rat model, Carbohydr. Polym. 231 (2020) 115734. https://doi.org/https://doi.org/10.1016/j.carbpol.2019.115734.

[63] B.K. Patel, R.H. Parikh, P.S. Aboti, Development of oral sustained release rifampicin loaded chitosan nanoparticles by design of experiment, J. Drug Deliv. 2013 (2013) 370938.

[64] H. Qiu, S. Cao, R. Xu, Cancer incidence, mortality, and burden in China: a time-trend analysis and comparison with the United States and United Kingdom based on the global epidemiological data released in 2020, Cancer Commun. 41 (2021) 1037–1048. https://doi.org/https://doi.org/10.1002/cac2.12197.

[65] K.-Y. Lu, R. Li, C.-H. Hsu, C.-W. Lin, S.-C. Chou, M.-L. Tsai, F.-L. Mi, Development of a new type of multifunctional fucoidan-based nanoparticles for anticancer drug delivery, Carbohydr. Polym. 165 (2017) 410–420. https://doi.org/https://doi.org/10.1016/j.carbpol.2017.02.065.

[66] P. Suyana, S. Nishanth Kumar, N. Madhavan, B.S. Dileep Kumar, B.N. Nair, A.P. Mohamed, K.G.K. Warrier, U.S. Hareesh, Reactive oxygen species (ROS) mediated enhanced anti-candidal activity of ZnS–ZnO nanocomposites with low inhibitory concentrations, RSC Adv. 5 (2015) 76718–76728. https://doi.org/10.1039/C5RA13316E.

[67] G. Enkhtaivan, D.H. Kim, M. Pandurangan, Cytotoxic effect of TDZ on human cervical cancer cells, J. Photochem. Photobiol. B Biol. 173 (2017) 493–498. https://doi.org/https://doi.org/10.1016/j.jphotobiol.2017.06.032.

[68] M.K.M. Subarkhan, R. Ramesh, Ruthenium(II) arene complexes containing benzhydrazone ligands: Synthesis, structure and antiproliferative activity, Inorg. Chem. Front. 3 (2016) 1245–1255. https://doi.org/10.1039/c6qi00197a.

[69] P. Tambe, P. Kumar, K.M. Paknikar, V. Gajbhiye, Decapeptide functionalized targeted mesoporous silica nanoparticles with doxorubicin exhibit enhanced apoptotic effect in breast and prostate cancer cells, Int. J. Nanomedicine. 13 (2018) 7669–7680. https://doi.org/10.2147/IJN.S184634.

[70] Z. Nie, D. Wang, S. Wang, L. Wang, Facile construction of irinotecan loaded mesoporous nano-formulation with surface-initiated polymerization to improve stimuli-responsive drug delivery for breast cancer therapy, Heliyon. 9 (2023) e15087. https://doi.org/https://doi.org/10.1016/j.heliyon.2023.e15087.

[71] L. Sethuram, J. Thomas, A. Mukherjee, N. Chandrasekaran, Effects and formulation of silver nanoscaffolds on cytotoxicity dependent ion release kinetics towards enhanced excision wound healing patterns in Wistar albino rats, RSC Adv. 9 (2019) 35677–35694. https://doi.org/10.1039/C9RA06913E.

Figures

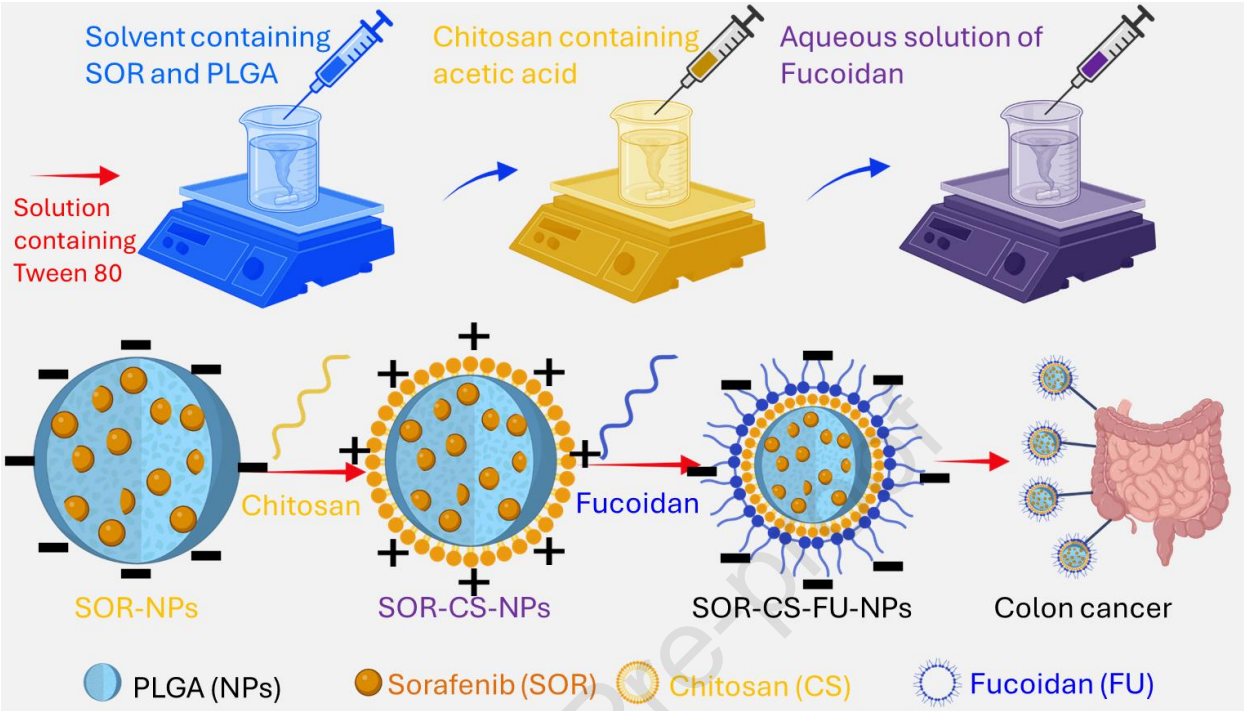

Figure 1. Graphical illustration of SOR-CS-FU-NPs fabrication method and targeted colon cancer cell delivery.

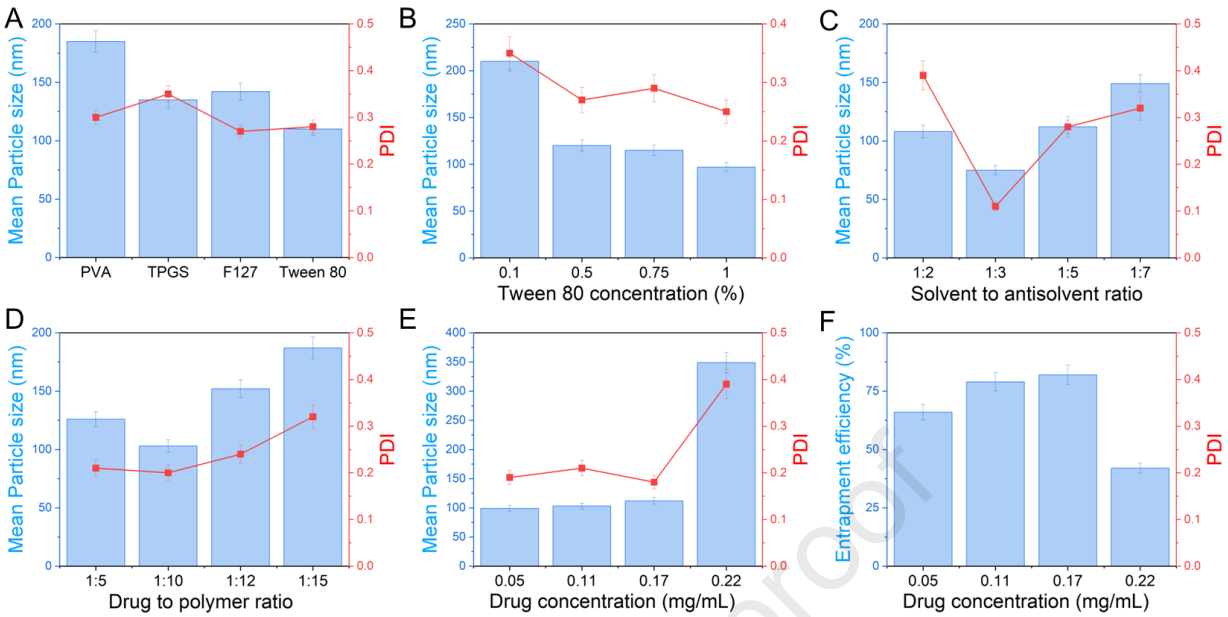

Figure 2. Measurements of SOR-NPs. A) Effect of various surfactants on particle diameter and PDI. B) Impact of surfactant dose on particle diameter and PDI. C) Impact of solvent to antisolvent rate on particle diameter and PDI. D) Result of drug to polymer's rate on particle diameter and PDI. E) Result of drug concentrations on diameter and PDI. F) Impact of drug concentrations on the EE (%).

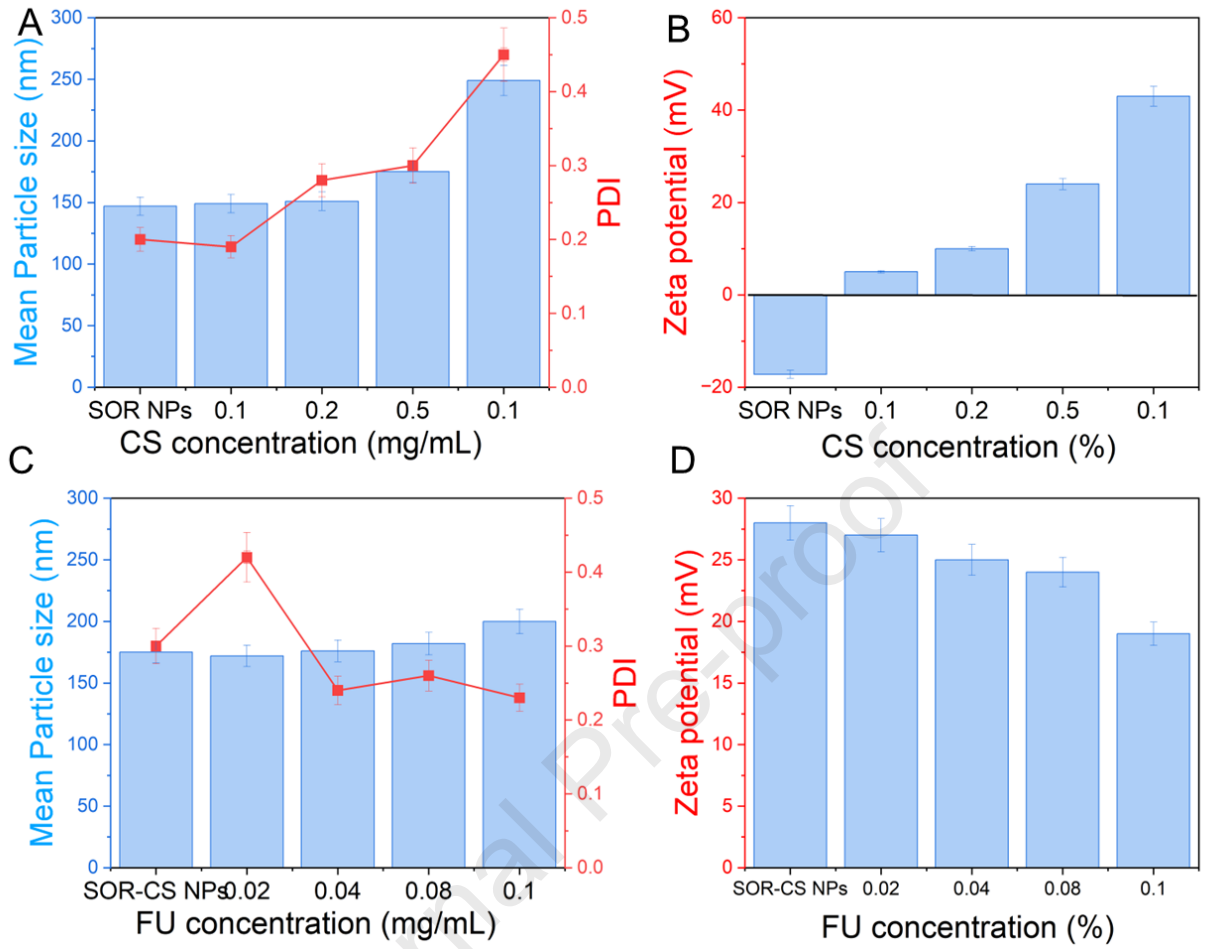

Figure 3. Coating measurements of SOR-NPs. A) Result of concentrations of CS on average particle diameter and PDI. B) Outcome of concentrations of CS layer on zeta potential. C) Result of concentration of FU on average particle diameter and PDI. D) Outcome of concentrations of FU layer on zeta potential.

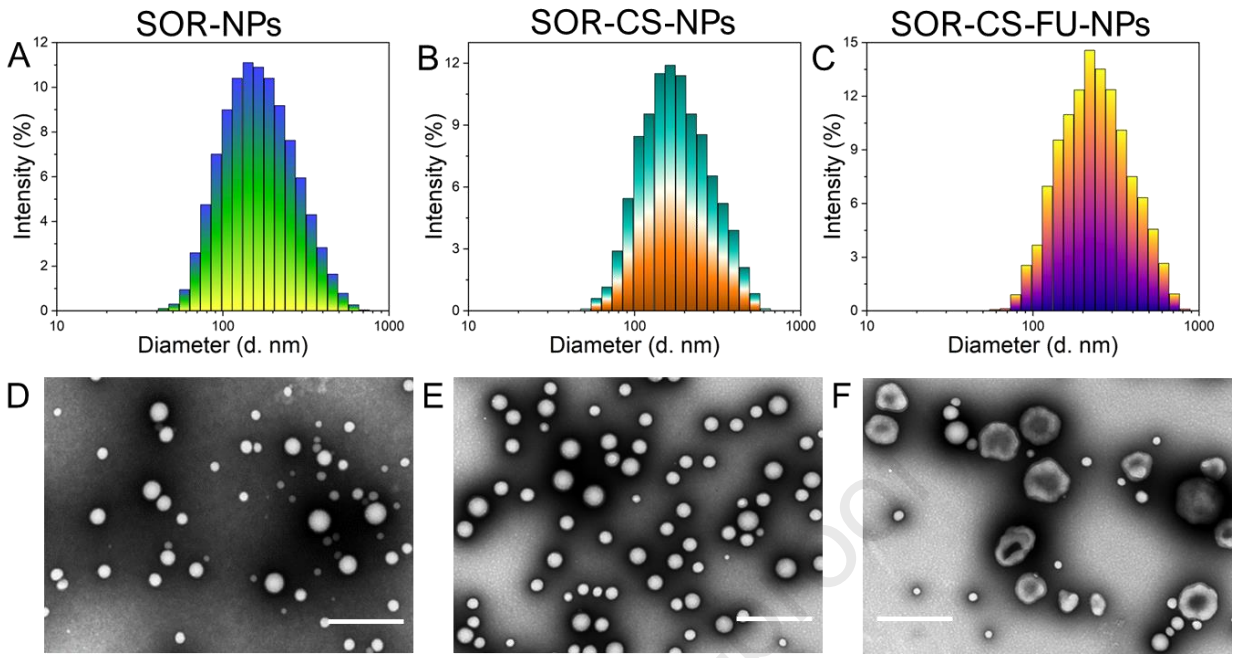

Figure 4. Morphological investigations of SOR-CS-FU-NPs. A-C) DLS measurements of SOR-NPs, SOR-CS-NPs, and SOR-CS-FU-NPs. D-F) TEM images of SOR-NPs, SOR-CS-NPs, and SOR-CS-FU-NPs.

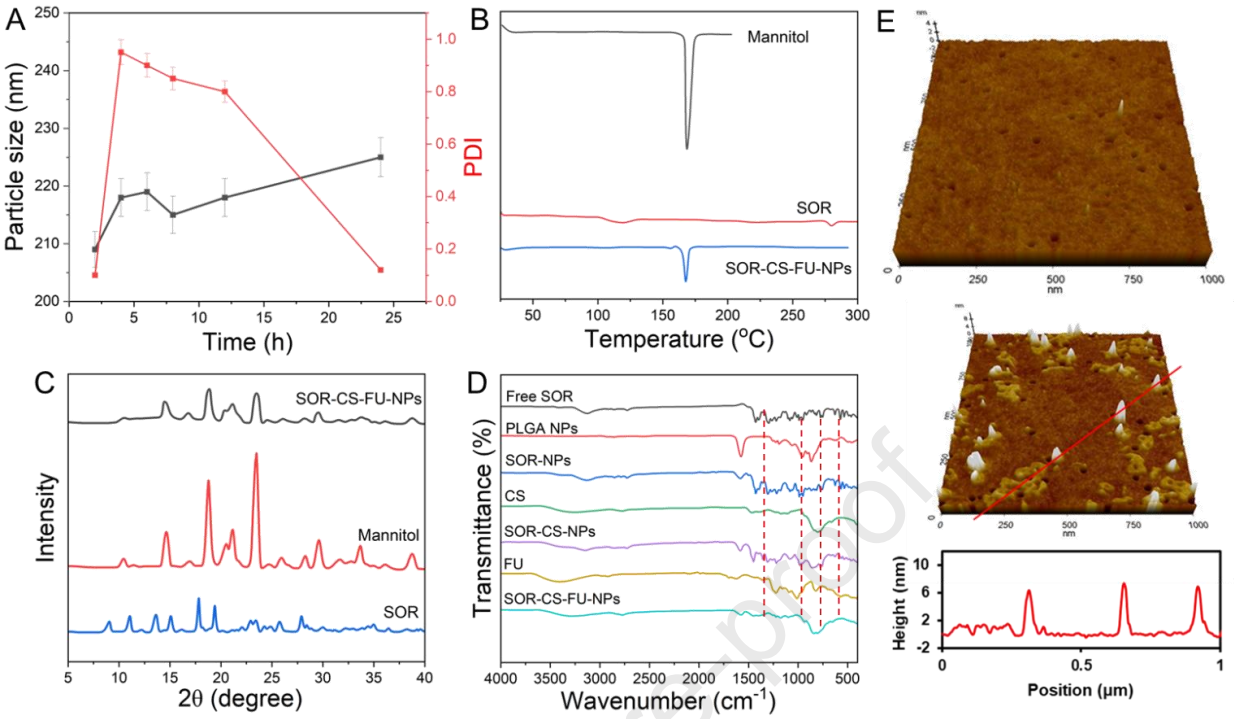

Figure 5. Characterization of SOR-CS-FU-NPs. A) Serum stability of SOR-CS-FU-NPs. B) DSC analysis of SOR-CS-FU-NPs. C) XRD profile of SOR-CS-FU-NPs. D) FTIR spectral analysis of various nanoparticles and coating of distinct components. E) Atomic force microscopy (AFM) analysis profile of SOR-CS-FU-NPs.

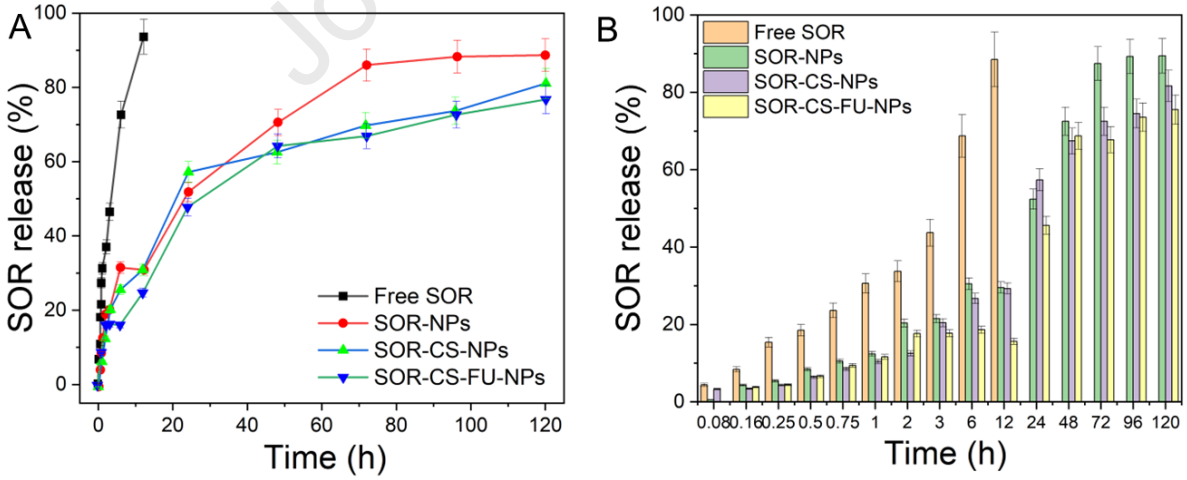

Figure 6. A) In vitro SOR release profile of SOR-CS-FU-NPs, SOR-CS-NPs, SOR-NPs and Free SOR. B) Various hours of DST release from SOR-CS-FU-NPs, SOR-CS-NPs, SOR-NPs and Free SOR.

881

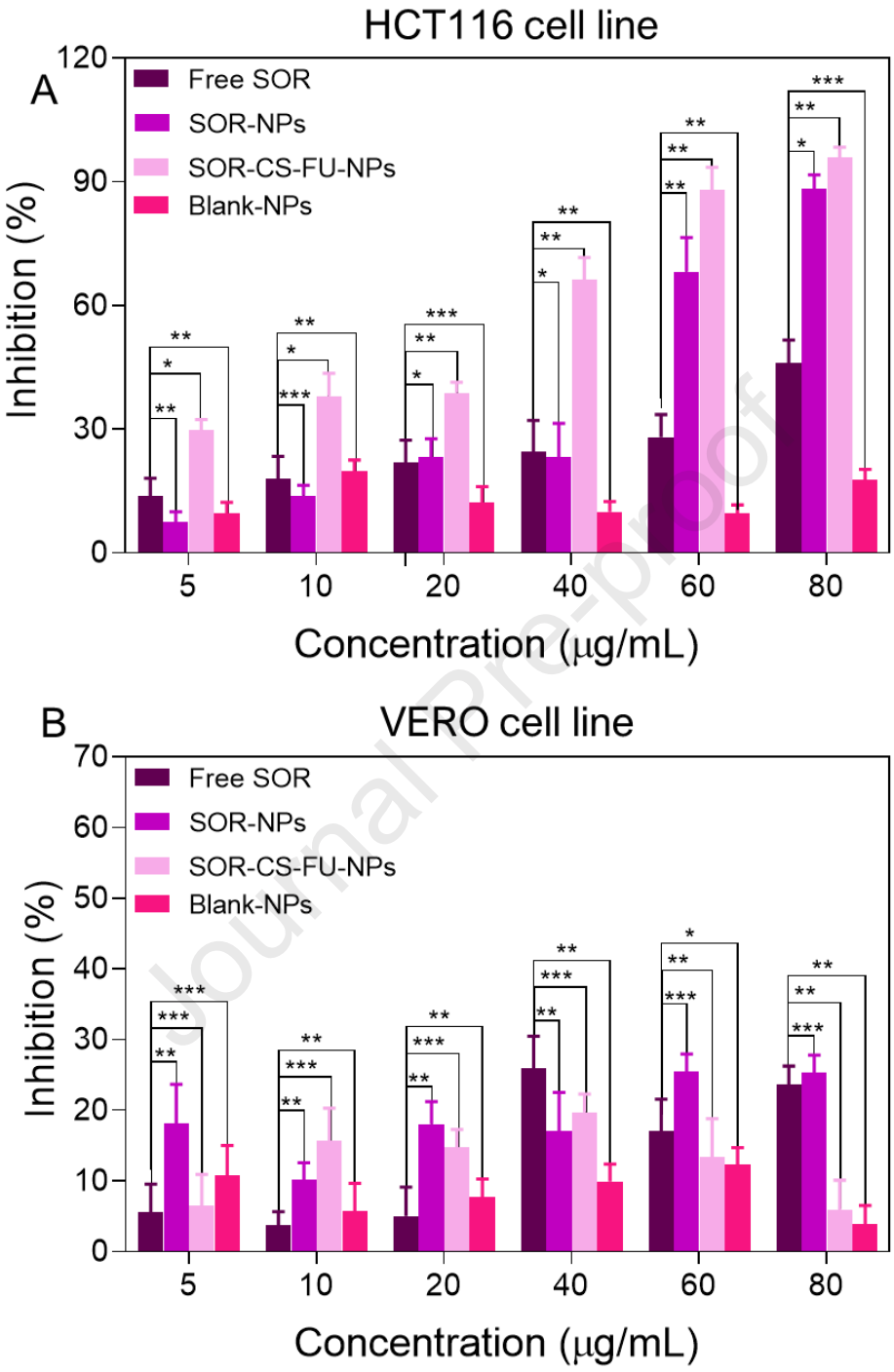

882

883 Figure 7. A) Inhibition of Blank-NPs, free Sor, SOR-NPs, and SOR-CS-FU-NPs on the
884 growth of HCT116 cells as investigated by MTT assay. B) Inhibition of Blank-NPs, free
885 Sor, SOR-NPs, and SOR-CS-FU-NPs on the growth of non-cancerous VERO cells as
886 investigated by MTT assay. Bars show each experiment's mean ± standard deviation
887 (n=3). p-value < 0.05, 0.01, and 0.001 were statistically significant difference with *, **,
888 and ***, respectively.

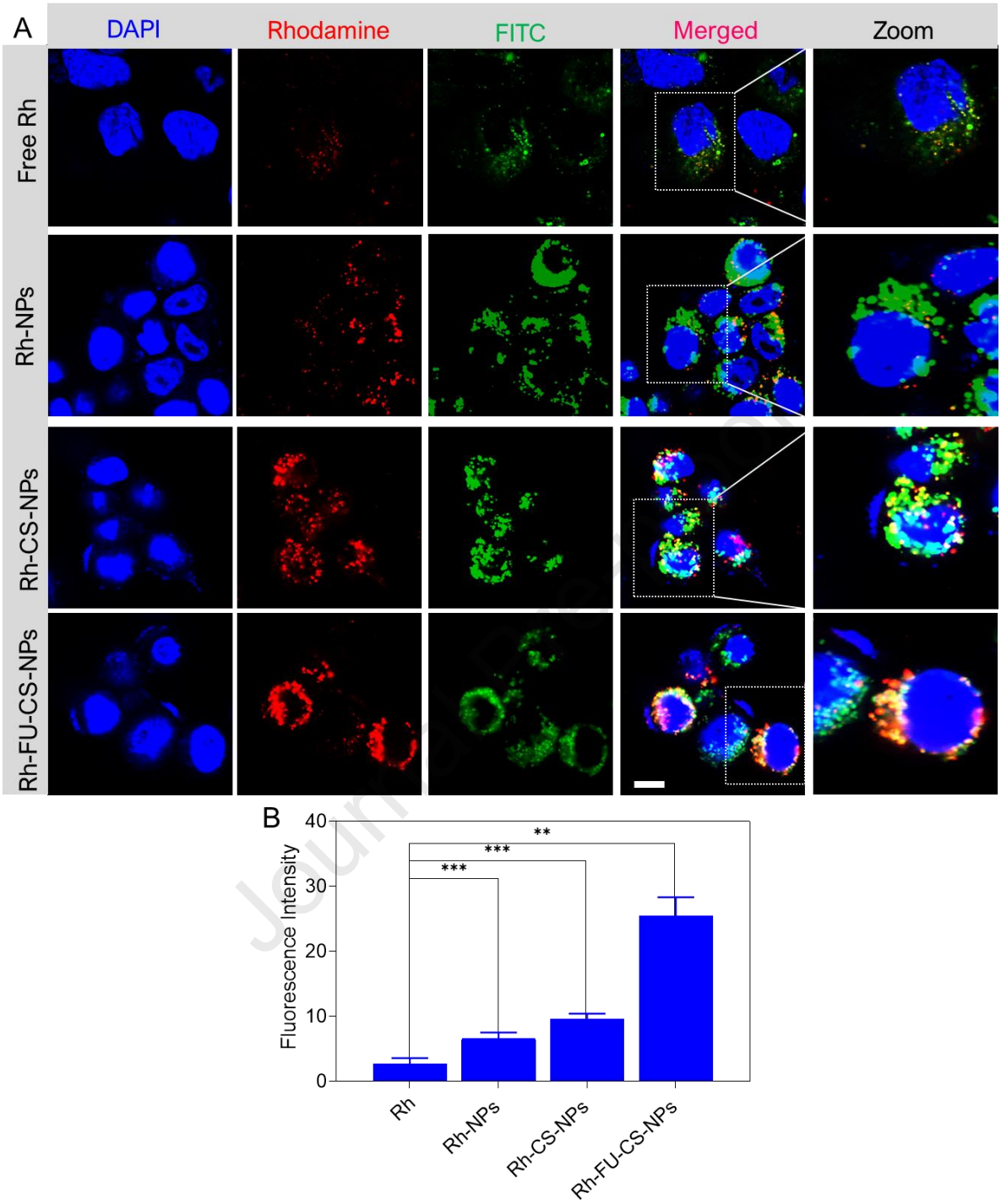

Figure 8. A) Confocal images of HCT116 cells subjected to free Rh and Rho-loaded NPs for cellular uptake qualitative investigations. B) Cell uptake quantitative analysis of HCT116 using ImageJ software. Bars show each experiment's mean ± standard deviation (n=3). p-value < 0.01, and 0.001 were statistically significant difference with **, and ***, respectively.

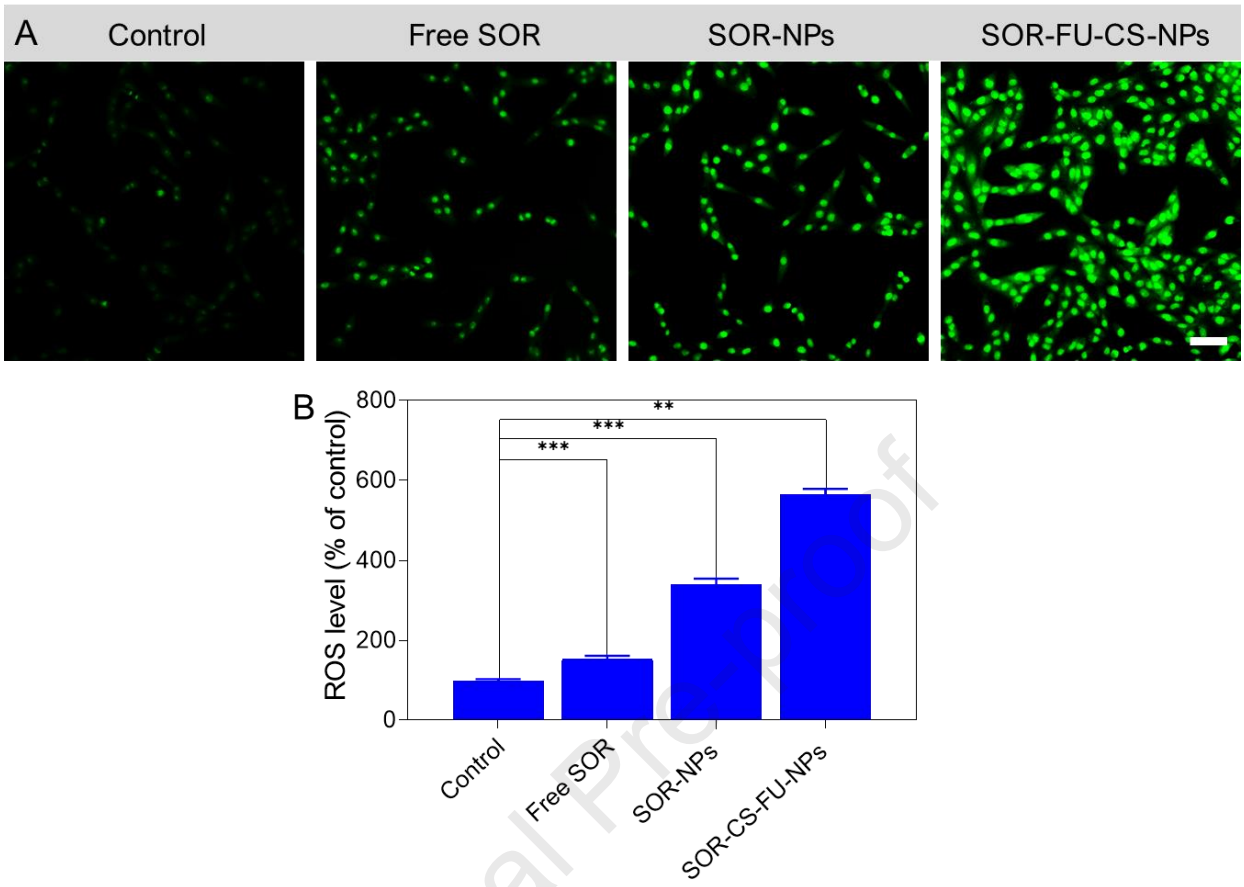

Figure 9. ROS generation of various treatment groups subjected to HCT116 cells. A) Fluorescence images of ROS measurement by DCF staining on HCT116 cells. B) Respective bar diagram quantified using ImageJ software. Bars show each experiment's mean ± standard deviation (n=3). p-value < 0.01, and 0.001 were statistically significant difference with **, and ***, respectively.

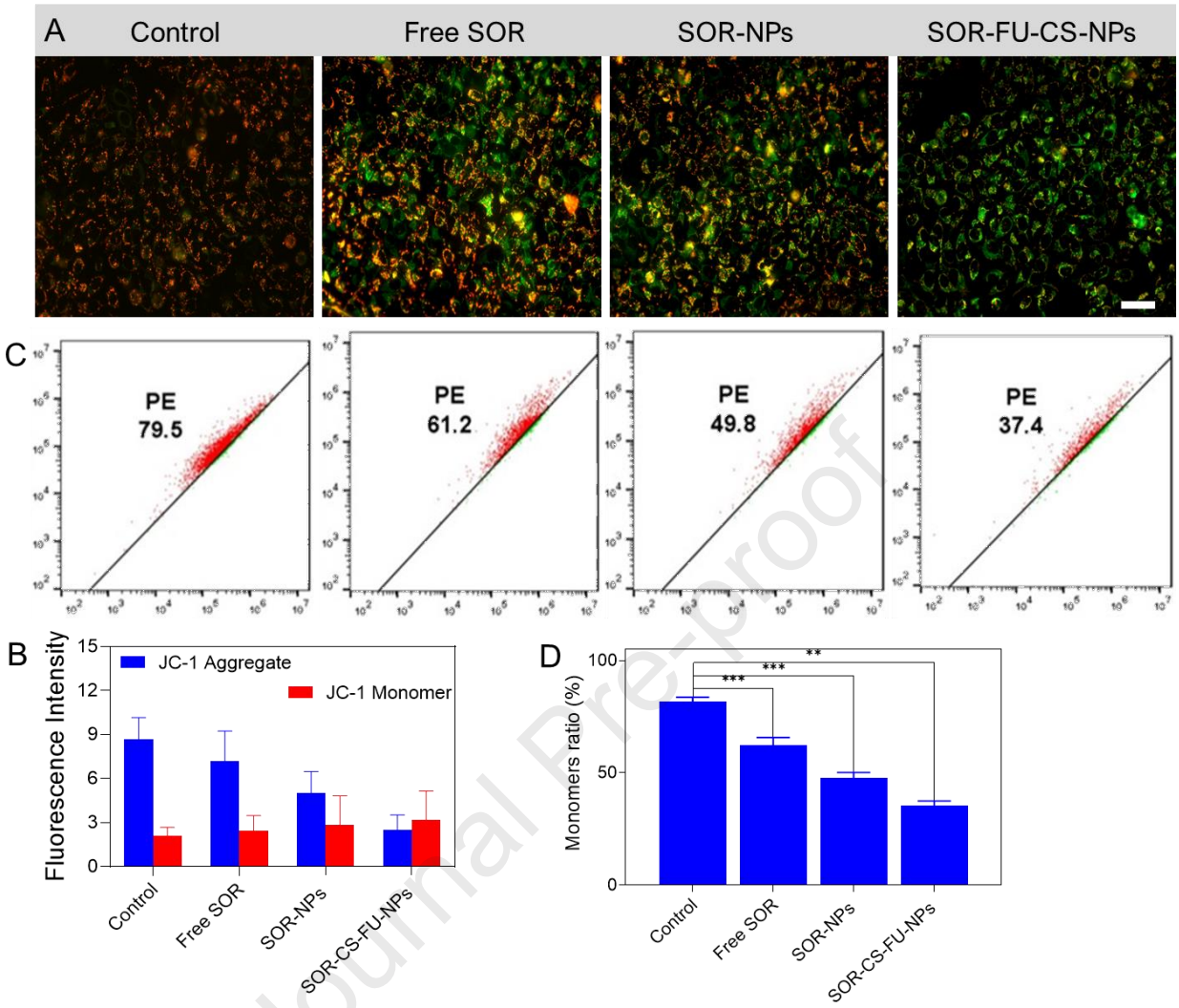

Figure 10. Mitochondrial membrane potential generation of various treatment groups subjected to HCT116 cells. A) Fluorescence and C) Flow cytometry images of ROS measurement by JC-1 staining on HCT116 cells. B) Respective bar diagram of fluorescence images. D) Respective bar diagram of flow cytometry images quantified using ImageJ software. Bars show each experiment's mean ± standard deviation (n=3). p-value < 0.01, and 0.001 were statistically significant difference with **, and ***, respectively.

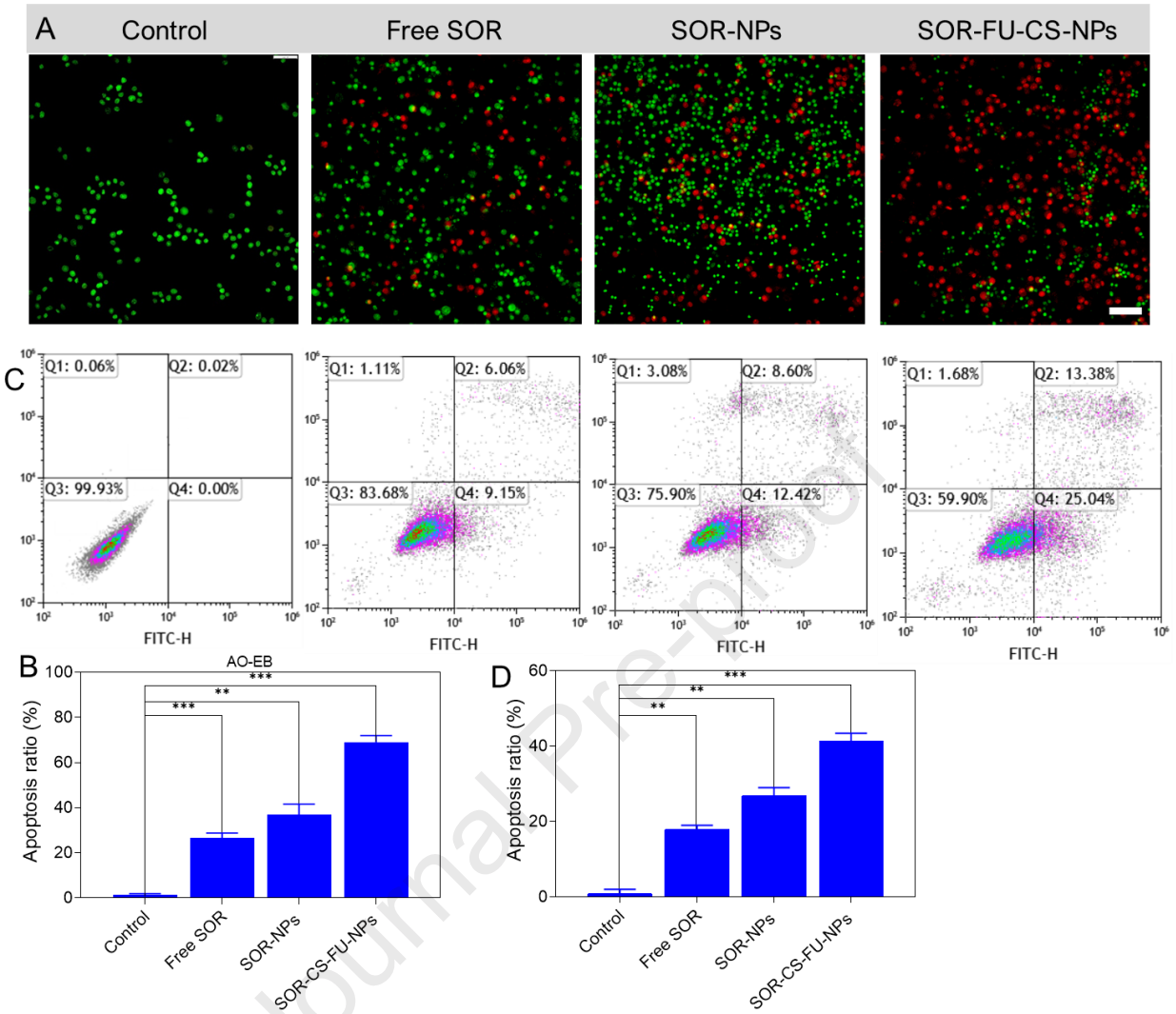

Figure 11. Acridine orange and ethidium bromide (AO/EB) and flow cytometry investigations were confirmed to examine the morphological investigations of various treatment groups subjected to HCT116 cells. A) Fluorescence and C) Flow cytometry images of apoptosis by Annuxin-V-FITC and PI staining on HCT116 cells. B) Respective bar diagram of fluorescence images quantified using ImageJ software. D) Respective bar diagram of flow cytometry images. Bars show each experiment's mean ± standard deviation (n=3). p-value < 0.01, and 0.001 were statistically significant difference with **, and ***, respectively.

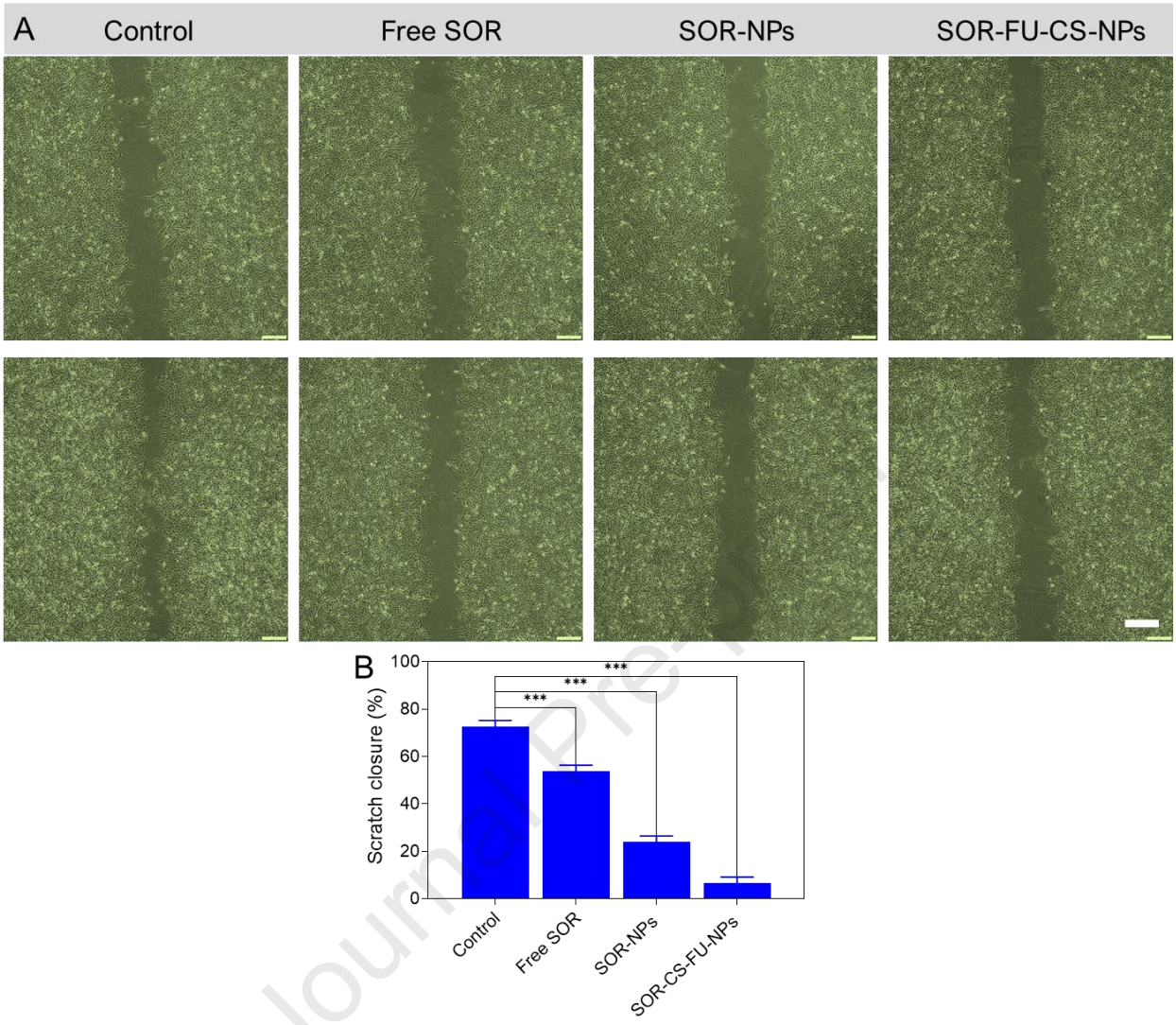

Figure 12. Wound scratch assay. A) Respective wound healing ability of the various NPs. B) Respective bar diagram of wound healing images. Bars show each experiment's mean ± standard deviation (n=3). p-value < 0.001 were statistically significant difference with ***, respectively.

Declaration of Competing Interest

The authors declare that they have no known competing financial interests.